Cell Reports
Medicine

Article

Effector T cell responses unleashed by regulatory T cell ablation exacerbate oral squamous cell carcinoma

Graphical abstract

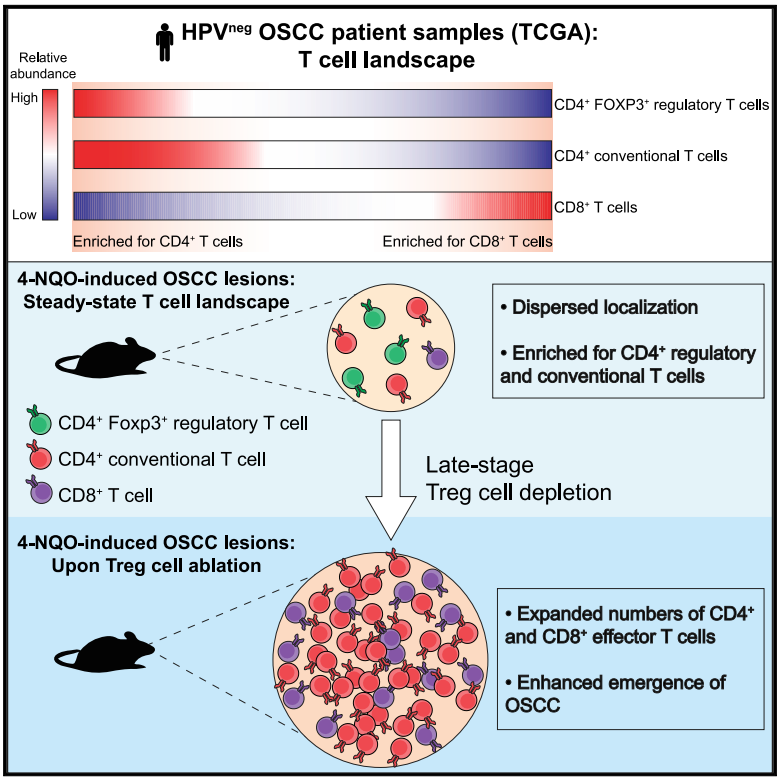

Highlights

- Human OSCCs are marked by polarized clusters of $CD8^+$ or $CD4^+$ T cell-enriched tumors
- In a mouse model of carcinogen-induced OSCC, late Treg cell ablation exacerbates OSCC
- Exacerbation of OSCC following Treg cell ablation is dependent on effector T cells

Authors

Jaime L. Chao, Michael Korzinkin, Alex Zhavoronkov, ..., Mark W. Lingen, Evgeny Izumchenko, Peter A. Savage

Correspondence

izumchen@medicine.bsd.uchicago.edu (E.I.),
psavage@bsd.uchicago.edu (P.A.S.)

In brief

Chao et al. demonstrate that HPV-negative oral squamous cell carcinomas (OSCCs) are characterized by polarized clusters enriched for $CD8^+$ or $CD4^+$ T cells. In a mouse model of carcinogen-induced OSCC, late-stage depletion of regulatory T cells promotes the emergence of invasive OSCCs via an effector T cell-dependent process.

Chao et al., 2021, Cell Reports Medicine 2, 100399
September 21, 2021
https://doi.org/10.1016/j.xcrm.2021.100399

CellPress

Cell Reports Medicine

CellPress
OPEN ACCESS

Article

Effector T cell responses unleashed by regulatory T cell ablation exacerbate oral squamous cell carcinoma

Jaime L. Chao,[1] Michael Korzinkin,[2] Alex Zhavoronkov,[2] Ivan V. Ozerov,[2] Matthew T. Walker,[1] Kathleen Higgins,[1] Mark W. Lingen,[1] Evgeny Izumchenko,[3,*] and Peter A. Savage[1,4,*]

[1]Department of Pathology, University of Chicago, Chicago, IL 60637, USA
[2]Insilico Medicine Hong Kong, Ltd., Pak Shek Kok, Hong Kong
[3]Department of Medicine, University of Chicago, Chicago, IL 60637, USA
[4]Lead contact
*Correspondence: izumchen@medicine.bsd.uchicago.edu (E.I.), psavage@bsd.uchicago.edu (P.A.S.)
https://doi.org/10.1016/j.xcrm.2021.100399

SUMMARY

Immune suppression by CD4$^+$FOXP3$^+$ regulatory T (Treg) cells and tumor infiltration by CD8$^+$ effector T cells represent two major factors impacting response to cancer immunotherapy. Using deconvolution-based transcriptional profiling of human papilloma virus (HPV)-negative oral squamous cell carcinomas (OSCCs) and other solid cancers, we demonstrate that the density of Treg cells does not correlate with that of CD8$^+$ T cells in many tumors, revealing polarized clusters enriched for either CD8$^+$ T cells or CD4$^+$ Treg and conventional T cells. In a mouse model of carcinogen-induced OSCC characterized by CD4$^+$ T cell enrichment, late-stage Treg cell ablation triggers increased densities of both CD4$^+$ and CD8$^+$ effector T cells within oral lesions. Notably, this intervention does not induce tumor regression but instead induces rapid emergence of invasive OSCCs via an effector T cell-dependent process. Thus, induction of a T cell-inflamed phenotype via therapeutic manipulation of Treg cells may trigger unexpected tumor-promoting effects in OSCC.

INTRODUCTION

In recent years, a broad conceptual framework has emerged for understanding the endogenous immune response to cancer and factors impacting the success or failure of immune-based cancer therapies.[1] The genetic and epigenetic changes associated with tumorigenesis can lead to tumor cell expression of mutated or aberrantly expressed proteins, which serve as the source of short peptide antigens that can be complexed with major histocompatibility complex (MHC) molecules and displayed at the cell surface for recognition by CD4$^+$ and CD8$^+$ T cells. Antigen-presenting cells acquire tumor-derived constituents and present peptide antigens to T cells in the draining lymph nodes. In cases in which productive T cell priming occurs, T cells undergo activation, proliferation, and differentiation, followed by exit from the lymph nodes and trafficking to the tumor site. There, effector T cells have the potential to induce tumor control via directed production of cytolytic effectors or local production of modulatory factors.

For many cancer types, a major fraction of tumors lack a substantial T cell infiltrate,[1–3] implying the lack of effective T cell priming in the lymph nodes, the exclusion of primed T cells from the tumor parenchyma, or limited survival of T cells within the tumor microenvironment. Clinical studies demonstrate that a paucity of intratumoral T cells is a major factor restricting the efficacy of checkpoint blockade antibodies targeting the PD-1 or CTLA-4 axes, as objective responses are largely restricted to "T cell-inflamed" tumors that harbor a high-density T cell infiltrate at baseline.[2,4–6] This has sparked considerable interest in understanding the mechanisms restricting T cell density within tumors and devising new strategies to induce a T cell-inflamed phenotype in otherwise "cold" neoplasms.

In this regard, a major focus has centered on understanding the biology of CD4$^+$ FOXP3$^+$ regulatory T (Treg) cells in the tumor setting. Treg cells are found at elevated densities within many human cancers and are thought to facilitate cancer progression and therapeutic resistance by suppressing the priming and activity of tumor-reactive effector T cells.[7–9] Consistent with these observations, intratumoral Treg cell density has been correlated with a poor prognosis for some cancer types.[10,11] However, studies in mice have demonstrated that Treg cells may serve diverse tissue-specific functions that are unrelated to effector T cell suppression, including metabolic regulation,[12,13] the promotion of tissue repair,[14,15] and the regulation of stem cell differentiation,[16] suggestive of multifaceted functions of intratumoral Treg cells within the tumor microenvironment. Importantly, intratumoral Treg cells express a panoply of cell-surface receptors that are targeted by current and emerging antibody-based therapies, including PD-1, CTLA-4, OX40, 4-1BB, TIM-3, Lag3, and GITR,[7,17–21] suggesting that tumor-infiltrating Treg cells are likely to be directly impacted by therapeutic antibodies and are therefore key determinants of therapeutic outcome.

Smoking-associated human papilloma virus (HPV)-negative head-and-neck squamous cell carcinomas (HNSCCs), which include many oral squamous cell carcinomas (OSCCs), represent an archetypal cancer that exhibits cardinal features of response or resistance to immune-based therapy, making it a compelling system for understanding the immunological forces that shape cancer development and response to therapy. Most HNSCCs harbor an elevated density of somatic point mutations[22–24] with potential to encode peptide neo-antigens. Notably, HPV-negative HNSCCs may arise from different anatomical sites and exhibit substantial genomic, phenotypic, and therapeutic heterogeneity, with the fraction of advanced HNSCCs that are responsive to anti-PD-1 and anti-PD-L1 checkpoint blockade largely restricted to those with a T cell-inflamed phenotype at baseline.[25] However, HPV-negative HNSCCs also exhibit compelling properties that are not aligned with the common conceptual framework of anti-tumor immunity. First, multiple prognostic studies reveal that high Treg cell density within the tumor center or tumor stroma is associated with a favorable prognosis in a subset of HNSCC patients,[26,27] a finding inconsistent with the notion that intratumoral Treg cells promote HNSCC and negatively impact clinical outcome by suppressing tumor-reactive effector T cells. Second, a study of HNSCC patients treated with anti-PD-1 or anti-PD-L1 therapy reported that over 25% of patients experienced "hyper-progression" characterized by accelerated tumor growth kinetics following therapy,[28] suggesting that checkpoint blockade may accelerate disease in a fraction of patients. These reports demonstrate that the processes governing endogenous anti-tumor immunity and the response to therapy are likely to vary based on host genetics, cancer genetics, the microbiota, the cell type of cancer origin, as well as the local tissue environment and highlight a critical need for mechanistic insight in tractable animal models that accurately mimic carcinogen-induced HNSCC development and progression.

Here, we utilize deconvolution-based profiling of human transcriptional data and mechanistic studies in a mouse model of autochthonous carcinogen-induced OSCC to investigate the relationship between two major determinants of response to immunotherapy—immune suppression by Foxp3$^+$ Treg cells and tumor infiltration by CD4$^+$ and CD8$^+$ effector T cells. Transcriptional profiling of HPV-negative OSCC, the most common type of HNSCC, and other cancers identified polarized clusters enriched for either CD8$^+$ T cells or CD4$^+$ Treg and conventional T cells, implying that the factors dictating the intratumoral density of CD8$^+$ T cells are distinct from those driving the density of Treg cells in many patients. In a mouse model of carcinogen-induced OSCC of the tongue, we found that induction of a strong T cell-inflamed phenotype via late-stage depletion of Treg cells did not induce tumor regression but instead induced rapid emergence of OSCCs via a process that was dependent on effector T cells. These mechanistic insights suggest that therapeutic intervention to manipulate intratumoral Treg cells or augment a T cell-inflamed phenotype may induce unexpected tumor-promoting effects, highlighting the importance of defining the mechanisms driving these effects and delineating biomarkers to identify HNSCC patients at risk of such adverse events.

RESULTS

In human subjects, the density of OSCC-infiltrating Treg cells does not correlate with CD8$^+$ T cell density in a subset of human tumors

Previous studies have suggested that the influx or expansion of FOXP3$^+$ Treg cells in human solid malignancies may be triggered in response to CD8$^+$ effector T cell infiltration and effector activity.[5,29] To examine this relationship in HPV-negative OSCC and other cancers, we used previously defined T cell-type-specific reference gene expression profiles from single-cell RNA sequencing[30] to estimate the relative abundance of CD4$^+$ Treg cells, CD4$^+$ conventional T cells, cytotoxic CD8$^+$ T cells, and exhausted CD8$^+$ T cells from bulk gene expression data derived from The Cancer Genome Atlas (TCGA) and Chicago Head and Neck Genomics Cohort (CHGC) datasets[31] by mathematical deconvolution using the iPANDA algorithm.[32–34] This analysis revealed that HPV-negative OSCCs are associated with a range of predicted densities of exhausted and cytotoxic CD8$^+$ T cells (Figures 1A and 1C), highlighting the known variability of CD8$^+$ T cell infiltration in OSCCs.[24,26,34–38] The analysis also demonstrated that the predicted density of CD4$^+$ Treg cells correlated with the density of CD4$^+$ conventional T cells (Figures 1B and 1D). Notably, unsupervised clustering based on the relative densities of the four T cell subtypes revealed polarized OSCC clusters enriched for either CD8$^+$ T cells or CD4$^+$ Treg and conventional T cells (Figures 1A and 1C). Similar clusters enriched for either CD8$^+$ T cells or Treg cells were also identified using the xCell cell type enrichment analysis platform[39] (Figure S1A) and were observed using iPANDA to analyze other human solid cancer types that are amenable to immune-based therapy (Figures S1B–S1I). These findings indicate that, in some tumors, the factors dictating the density of intratumoral CD4$^+$ T cells (Treg cells and/or CD4$^+$ T conventional cells) are likely to be distinct from the determinants of CD8$^+$ T cell density and suggest that tumor infiltration by CD8$^+$ T cells is unlikely to be a primary determinant of intratumoral Treg cell density in such cancers.

Murine carcinogen-induced oral lesions are associated with a low-density T cell infiltrate polarized toward enrichment of CD4$^+$ T cells

The above findings, paired with prognostic studies indicating that high Treg cell density is associated with a favorable prognosis in OSCCs and some other human cancers,[10,11,24,26,27,35,38,40–42] illustrate compelling correlates that may have functional significance for understanding anti-tumor immunity and response to immunotherapy. A clear understanding of the significance of these relationships requires mechanistic loss- and gain-of-function experiments in animal models that accurately recapitulate the biology of OSCC. With this in mind, we utilized a mouse model of carcinogen-induced OSCC to gain a better understanding of the nature of Treg cells associated with these neoplasms and to define the relationship between Treg cells and effector T cells in this setting. In this model, mice are exposed to drinking water containing the chemical carcinogen 4-nitroquinoline N-oxide (4-NQO) for 20 weeks to induce oral lesions in the tongue epithelium.[43–47] Notably, the progression and histopathology of 4-NQO-induced lesions in mice closely mirror that of HPV-negative

CellPress
OPEN ACCESS

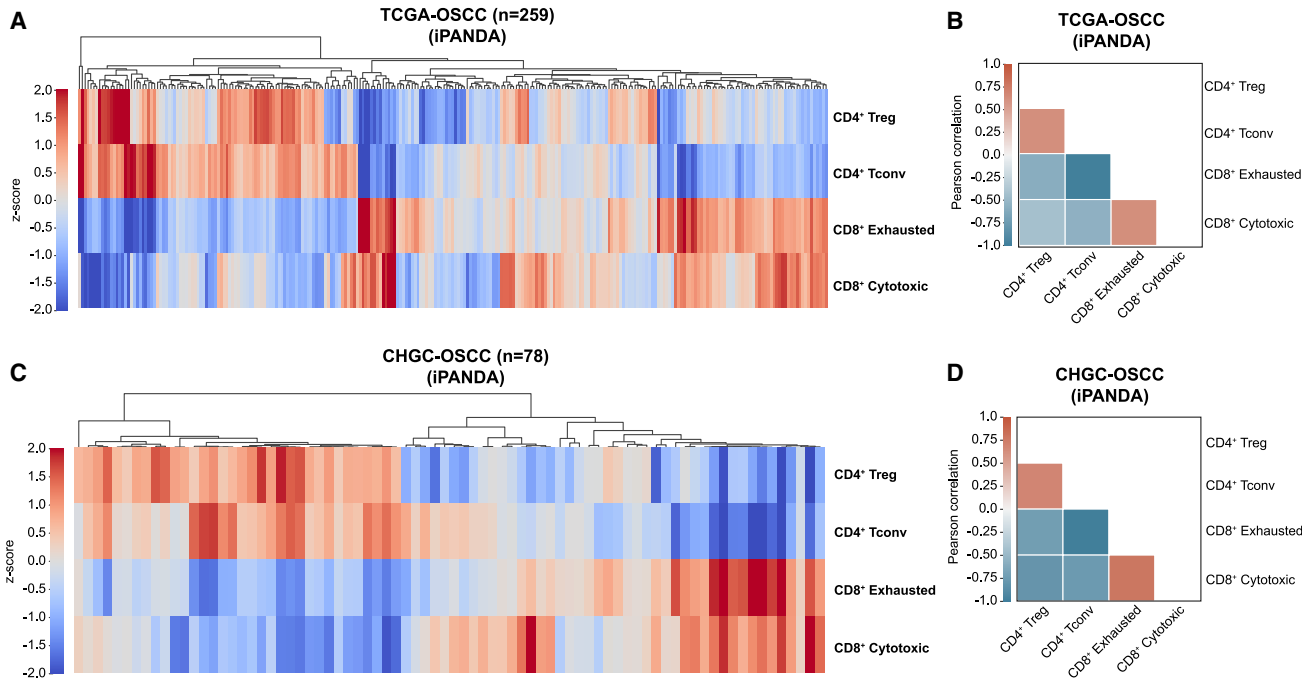

Figure 1. In human subjects, the density of OSCC-infiltrating Treg cells does not correlate with CD8$^+$ T cell density in a subset of human tumors

Heatmap of Z scores depicting the relative abundance of CD4$^+$ Treg cells, CD4$^+$ conventional T cells, cytotoxic CD8$^+$ T cells, and exhausted CD8$^+$ T cells from bulk gene expression data using the iPANDA algorithm.

(A and C) Heatmaps of HPV-negative OSCC datasets derived from (A) The Cancer Genome Atlas (TCGA) or (C) Chicago Head and Neck Genomics Cohort (CHGC) displaying the normalized Z scores of the relative abundance of CD4$^+$ Treg cells, CD4$^+$ conventional T cells, cytotoxic CD8$^+$ T cells, and exhausted CD8$^+$ T cells. Each column represents an individual patient sample. Color denotes the normalized Z score. Unsupervised clustering is used.

(B and D) Correlation plots displaying pairwise comparisons of each T cell subset from (B) TCGA or (D) CHGC datasets. Color denotes the Pearson correlation score.

n = 259 samples (TCGA) and 78 samples (CHGC). See also Figure S1.

OSCC, including characteristic progression from pre-neoplastic dysplasia to invasive OSCC.[43,46,48–50] Previous studies using this model report an OSCC incidence ranging from 10% to 50%, depending on the duration and dose of 4-NQO exposure.[45,47] We developed an approach to quantitatively assess 4-NQO-induced lesions of the tongue with respect to the incidence and burden of lesions of distinct histological grades (Figures 2A–2C). Following longitudinal tongue bisection, tissue sections from the mid-plane were stained with H&E and blinded. The epithelial perimeter of each tongue section was then traced, and the fraction of the perimeter characterized by distinct histological grades (normal epithelium, hyperkeratosis, dysplasia, or invasive OSCC; Figure 2A) was quantified and plotted for each mouse using two approaches. As illustrated for a cohort of ten 4-NQO-treated mice in Figures 2B and 2C, all mice developed hyperkeratosis and dysplastic lesions by 20 weeks of carcinogen exposure, with 4 mice developing invasive OSCC (Figures 2B and 2C). Collectively, 37% of wild-type mice exposed to 4-NQO for 20 weeks developed OSCC in this study.

To understand the endogenous immune response in this model, we analyzed the nature of T cell subsets infiltrating 4-NQO-induced oral lesions. Analysis using immunohistochemistry (IHC) revealed that CD3$^+$ T cells were detected at low densities within most 4-NQO-induced dysplasias and OSCCs and that these densities were slightly elevated relative to normal epithelium and regions of hyperkeratosis (Figures 2D and 2E). T cells were sparse and typically localized near the basal epithelium or interspersed within the parenchyma of dysplastic and OSCC lesions (Figure 2D). Flow-cytometry-based analysis of tongue-associated T cells from either the whole tongue or from excised macroscopic lesions of undefined histology of 4-NQO-treated mice revealed the presence of CD8$^+$ T cells, CD4$^+$ conventional T cells, and CD4$^+$Foxp3$^+$ Treg cells (Figures 2F and 2G). In all cases examined, CD4$^+$ T cells were more abundant than CD8$^+$ T cells (Figure 2H), congruent with previous surveys of immune populations resident in the oral cavity.[51,52] In contrast, $\gamma\delta$ T cells were uncommon in whole tongues and excised lesions of 4-NQO-treated mice (data not shown; Figures S3A and S3B). On average, Foxp3$^+$ Treg cells accounted for 54% $\pm$ 18% of tongue-associated CD4$^+$ T cells isolated from 4-NQO-treated mice (Figure 2I), consistent with reports showing that human OSCCs harbor elevated percentages of FOXP3$^+$ Treg cells.[24,26,35] These Treg cells did not express lineage-defining transcription factors of differentiated helper T cell subsets, including T-bet, Gata3, and RORγt (Figure 2J), as has been described in some murine tumor models and human cancer patients.[53–56] Together, these data reveal that 4-NQO-induced lesions are characterized by low-density T cell

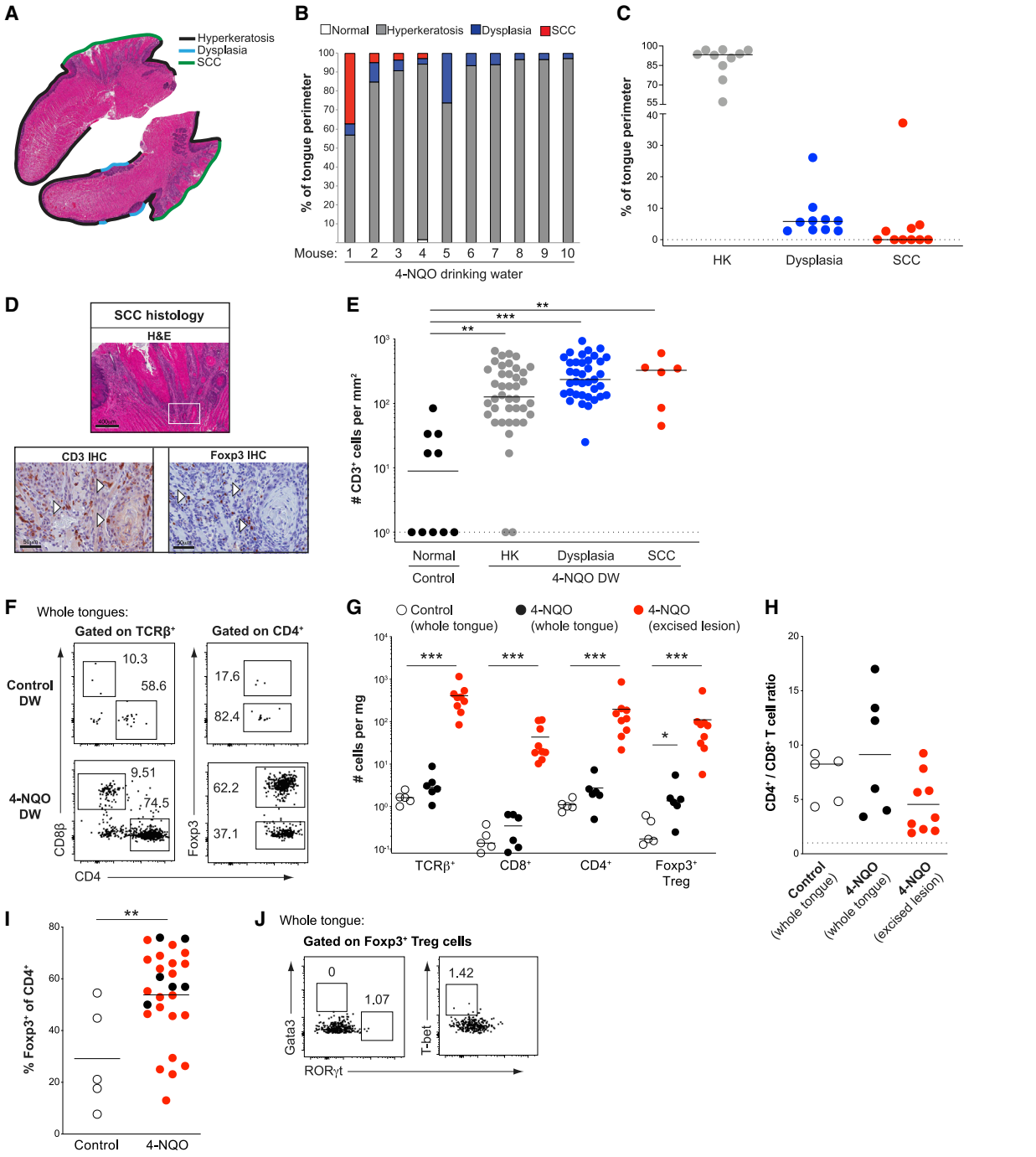

Figure 2. Murine carcinogen-induced oral lesions are enriched for CD4⁺ Treg and conventional T cells

6- to 8-week-old C57BL/6 mice were exposed to drinking water containing 100 μg/mL 4-NQO or vehicle control for 20 weeks.

(A) Quantification of histopathology. After 20 weeks of treatment with 4-NQO drinking water, tongues were dissected, fixed in 10% formalin, bisected longitudinally, and stained with H&E. The perimeter of each tongue is outlined and categorized base on histology grade: hyperkeratosis (black); dysplasia (blue); or SCC (green). Shown is a representative H&E stain of FFPE tongue after longitudinal bisection of 4-NQO-treated mouse, perimeter traced based on histology grades noted above.

(B and C) Summary plots of 4-NQO-induced histopathology, showing the percentage of tongue perimeter defined as indicated histology grade. Each bar (B) or symbol (C) represents an individual tongue from a single mouse. Median is indicated in (C). n = 10 mice.

(D) (Top) Representative H&E image of SCC region of tongue epithelium from (A). (Bottom) Representative CD3 (left) and Foxp3 (right) IHC images of adjacent sections of depicted SCC region denoted by white box in H&E image are shown. White arrows denote CD3⁺ or Foxp3⁺ cells. Scale bars represent 400 μm (H&E) or 50 μm (IHC).

(legend continued on next page)

infiltration polarized toward enrichment of CD4$^+$ Treg and conventional T cells.

A fraction of tongue-associated Treg cells exhibit clonal expansion and reactivity to regional antigens

To gain insight into the antigen specificity of tongue-associated Treg cells in this model, we performed single-cell sorting of Treg cells isolated from whole tongues of 4-NQO-treated mice, followed by nested PCR amplification and sequencing of rearranged T cell receptor (TCR) genes.[57] To facilitate this analysis, we utilized mice expressing a *Foxp3*^{GFP} reporter allele and a fixed transgenic TCRβ (TCRβtg) chain,[58] which enables the analysis of TCR specificity and diversity by sequencing of the TCRα chain alone.[59,60] Our survey of Treg cells from five 4-NQO-treated *Foxp3*^{GFP} TCRβtg mice demonstrated that tongue-associated Treg cells from each mouse expressed a diverse array of TCRα chains (Figure 3A). Although the overall repertoire was diverse, a small fraction of tongue-associated Treg cell clones were found recurrently in multiple mice; seven clones were found in at least three of the five animals analyzed (Figure 3B). These recurrent clones expressed distinct CDR3α sequences and utilized diverse Vα and Jα elements (Table S1). Analysis of the representation of these TCRs in previously published TCRα datasets of T cells from the pooled secondary lymphoid organs (SLOs) of untreated tumor-free *Foxp3*^{GFP} TCRβtg mice[59] revealed that most TCRs expressed by tongue-associated Treg cells were preferentially expressed by Treg cells found in tumor-free mice (Figures 3A and 3B), suggesting that tongue-associated Treg cell clones in 4-NQO-treated mice were likely drawn from a pre-existing Treg cell pool.

To define the nature of antigens recognized by these recurrent Treg cell clones, we generated monoclonal TCR "retrogenic" (TCRrg) mice[60,61] expressing single recurrent tongue-associated Treg cell TCRs identified above. CD4$^+$ T cells from TCRrg mice were purified and co-transferred with congenically disparate polyclonal splenocytes into T cell-deficient *Tcrb*$^{-/-}$ recipient mice that had not been exposed to 4-NQO, and the distribution and activation status of donor TCRrg cells was assessed. For three of the four clones, TCRrg CD4$^+$ T cells exhibited preferential activation and/or accumulation in the tongue-draining cervical lymph nodes (cLNs) (Figures 3C and 3D), suggestive of reactivity to regional antigens that are presented in tumor-free animals, irrespective of tumor status and 4-NQO exposure.

4-NQO-induced lesions are not significantly impacted by the endogenous T cell response or treatment with checkpoint blockade monotherapies

Given that 4-NQO-induced lesions mimic genetic heterogeneity of human tobacco-associated OSCC[62] and harbor a high density of point mutations with potential to encode tumor-specific neoantigens,[49,50] we hypothesized that the endogenous T cell response may restrict the emergence of dysplasia or OSCC, as has been suggested for cancers exhibiting a high mutational load.[63] However, our data revealed that the incidence and burden of dysplasias and OSCCs were not significantly altered in αβ T cell-deficient *Tcrb*$^{-/-}$ mice or γδ T cell-deficient *Tcrd*$^{-/-}$ mice relative to wild-type littermates (Figures 4A and 4B), indicating that T cells do not measurably impact the emergence of 4-NQO-induced lesions in the absence of immune-based therapy. Of note, control experiments demonstrated that exposure to 4-NQO did not impair the T cell response elicited by immunization with a foreign peptide plus adjuvant (Figure S2A), indicating that 4-NQO exposure does not induce broad immune suppression.

To define the extent to which 4-NQO-induced lesions are responsive to established antibody-mediated checkpoint blockade immunotherapies, we treated 4-NQO-exposed mice with monotherapy using anti-PD-L1, anti-PD-1, or anti-CTLA-4 antibody, each paired with appropriate isotype control groups. As shown in Figures 4C, 4D, S2C, S2D, S2F, and S2G, these monotherapies did not significantly alter the burden or incidence of pre-neoplastic lesions or OSCCs and failed to significantly alter the density of infiltrating T cells (Figures 4E, S2E, S2H, and S2I), suggesting that 4-NQO-induced lesions were largely resistant to these T cell-directed checkpoint blockade monotherapies in the animal cohorts examined. While the factors underlying the negligible impact of αβ T cell deficiency or checkpoint blockade monotherapy remain undefined, we hypothesized that a lack of a high-density, tumor-infiltrating effector T cell response and a preponderance of suppressive Foxp3$^+$ Treg cells may promote therapeutic resistance.

Late-stage Treg cell depletion enhances the emergence of invasive OSCC

The above results suggest that the 4-NQO-induced model of OSCC mirrors a substantial fraction of human OSCCs and other common human malignancies, in which cancer lesions are associated with a low density of infiltrating T cells and do not exhibit

(E) Summary plot of pooled data from CD3 IHC density analysis, showing the number of CD3$^+$ cells per mm^2 for each lesion. Each symbol represents an individual lesion. Median is indicated. n = 10 regions from 1 mouse (control); n = 6–40 lesions from 10 mice (4-NQO).

(F) Representative flow cytometric analysis of CD8$^+$ and CD4$^+$ T cells isolated from tongues of 4-NQO-treated or vehicle-treated mice. Left plots depict CD4 versus CD8β expression by TCRβ$^+$ cells, whereas the right plots depict CD4 versus Foxp3 expression by CD4$^+$ T cells. The frequency of cells within the indicated gates is denoted.

(G–I) Summary plot of pooled data from (F), showing the number of TCRβ$^+$, CD8$^+$, CD4$^+$, or Foxp3$^+$ T cells per mg of tissue (G), the ratio of CD4$^+$ to CD8$^+$ T cells (H), or the frequency of Foxp3$^+$ cells among CD4$^+$ T cells (I) isolated from whole tongues of vehicle-treated mice (open circles), whole tongues from 4-NQO-treated mice (black circles), or excised tongue lesions from 4-NQO-treated mice (red circles). Each symbol represents an individual mouse (open and black circles) or an individual lesion (red circles). Mean is indicated. Dotted line represents ratio = 1 (H). n = 5 (control whole tongues), n = 6 (4-NQO whole tongues), and n = 9–21 (4-NQO excised lesions).

(J) Representative flow cytometric analysis of Foxp3$^+$ Treg cells isolated from tongue of 4-NQO-treated mouse. Left plot depicts RORγt versus Gata3 expression, whereas the right plot depicts RORγt versus T-bet expression. The frequency of cells within the indicated gates is denoted.

Data are pooled from multiple independent experiments. DW, drinking water; HK, hyperkeratosis; SCC, squamous cell carcinoma. One-way ANOVA with Dunn's post-test analysis, comparing all pairs in column (E; adjusted p values from Dunn's post-test are depicted); two-tailed nonparametric Mann Whitney test (G and I). *p < 0.0.5, **p < 0.01, and ***p < 0.001.

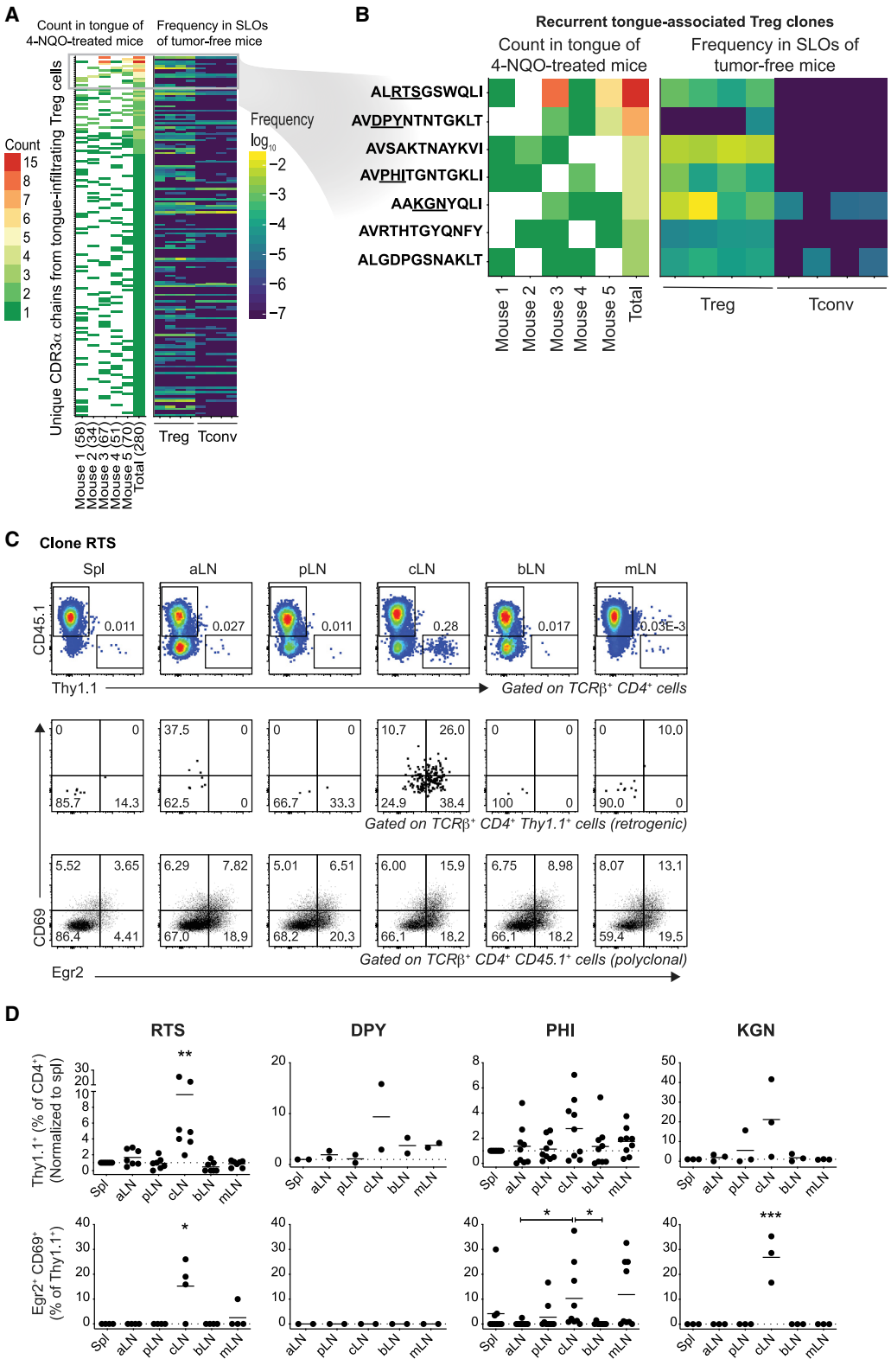

(legend on next page)

robust responses following checkpoint blockade therapy.[2,4,6,25,64] In this regard, a major therapeutic goal is to develop novel approaches to drive increased densities of tumor-infiltrating T cells, thereby turning non-T cell-inflamed "cold" tumors into T cell-inflamed "hot" tumors.[2,4–6] To examine this idea mechanistically, we aimed to augment effector T cell infiltration of 4-NQO-induced lesions by transiently ablating Foxp3$^+$ Treg cells, which has been previously shown to enhance intratumoral T cell density and promote tumor regression in some murine cancer models.[65–68] To this end, we utilized *Foxp3*$^{DTR/y}$ mice in which the human diphtheria toxin receptor (DTR) is expressed by all Foxp3-expressing cells, enabling inducible ablation of Treg cells via intraperitoneal administration of diphtheria toxin (DT). We exposed *Foxp3*$^{DTR/y}$ and control *Foxp3*$^{WT/y}$ male littermates to 4-NQO for 20 weeks. Starting at 16 weeks of 4-NQO exposure, Treg cells were ablated via DT administration for 1 week, and mice were then given 3 weeks to recover (Figure 5A). Of note, while DT-mediated Treg cell depletion was systemic,[69] mice did not develop adverse autoimmune reactions in non-lymphoid organs (data not shown), similar to previously reported results using a similar regimen.[65]

Unexpectedly, depletion of Treg cells at this late stage did not trigger regression of dysplastic lesions or OSCCs but instead induced increased incidence and burden of OSCCs within the short 4-week period following initiation of Treg cell ablation (Figures 5B and 5C). By IHC, increased OSCC incidence and burden were associated with a >2.5-fold increase in the densities of CD3$^+$ T cells in both dysplasias and OSCCs at endpoint (Figures 5D and 5E). In Treg-depleted *Foxp3*$^{DTR/y}$ mice, CD3$^+$ T cells were found in distinct clusters in both the basal epithelium and within the tumor parenchyma, compared to the sparse localization in lesions from DT-treated *Foxp3*$^{WT/y}$ littermates (Figure 5D). Notably, Foxp3$^+$ Treg cell densities within 4-NQO-induced lesions returned to baseline levels at the 20-week endpoint (4 weeks after initiation of Treg cell ablation; Figure 5F), highlighting the robust mechanisms driving Treg cell recovery following inducible depletion. Flow-cytometry-based analysis of the whole tongues of treated mice revealed that Foxp3^{neg} CD4$^+$ and CD8$^+$ αβ effector T cells were the major immune cell populations to increase in the tongues following Treg cell depletion (Figures 5G–5I), with other tongue-infiltrating CD45$^+$ cell populations remaining largely unaltered (Figures S3A and S3B). To determine whether Treg cell depletion had a similar impact during the earlier stages of carcinogenesis, we depleted Treg cells in a transient and periodic manner by administrating DT on consecutive days starting at 8 weeks of 4-NQO exposure and repeated every 3 weeks (Figure S3C). We found that this regimen induced elevated densities of CD3$^+$ T cells and Foxp3$^+$ Treg cells at the endpoint (Figures S3D and S3E) but did not have a significant effect on OSCC incidence or burden (Figures S3F and S3G), suggesting that the impact of Treg cell ablation is dependent on the time of depletion along the continuum of cancer progression. Cumulatively, these data reveal the unexpected finding that transient Treg cell depletion at the later stages of carcinogenesis enhances the emergence of OSCC.

Increased incidence and burden of OSCC following late-stage Treg cell depletion are dependent on effector T cells

Given that αβ effector T cells were the major immune population to significantly expand following Treg cell depletion (Figures 5G–5I), we next asked whether effector T cells were required for the enhanced emergence of OSCC in this setting. To test this, starting at 16 weeks of 4-NQO exposure, *Foxp3*$^{WT/y}$ and *Foxp3*$^{DTR/y}$ mice were treated with DT for 1 week to transiently ablate Treg cells plus concurrent anti-CD4 and anti-CD8 depleting antibodies or isotype control antibodies (Figure 6A). In mice treated with DT plus isotype control antibodies, Treg cell ablation led to elevated incidence and burden of OSCCs compared to non-depleted controls (Figures 6B and 6C; compare data columns

Figure 3. A fraction of tongue-associated Treg cell clones exhibit clonal expansion and reactivity to regional antigens

(A and B) 6- to 8-week-old *Foxp3*^{GFP} TCRβtg$^+$ mice were placed on 4-NQO drinking water for 8 weeks, followed by 24 weeks of normal drinking water. Treg cells were subsequently isolated from tongues, single-cell sorted by fluorescence-activated cell sorting (FACS), and TCRα chains were amplified by nested PCR and subjected to Sanger sequencing (see STAR Methods). n = 5 mice.

(A) Heatmap depicting all CDR3α sequences identified among all single-cell sorted Treg cells. Each row represents a unique CDR3α sequence. (Left) The number of occurrences each CDR3α sequence appears in tongue-associated Treg datasets from individual 4-NQO-treated mice is shown. Each column represents an individual mouse, with the number of cells sequenced per mouse noted in parentheses. The last column represents the cumulative data. Color denotes the total number each CDR3α sequence appears in dataset. (Right) The frequency each CDR3α sequence appears in published datasets of CD4$^+$ Foxp3$^+$ Treg cells or CD4$^+$ Foxp3^{neg} Tconv cells isolated from pooled secondary lymphoid organs (SLOs) of untreated, non-tumor-bearing *Foxp3*^{GFP} TCRβtg$^+$ mice is shown.[59] Each column represents dataset from an individual mouse. Color denotes the frequency of each CDR3α sequence in dataset.

(B) Select CDR3α sequences from (A), depicting those recurrent among at least three 4-NQO-treated mice. Underlined amino acid sequence refers to the 3-letter ID used to reference each TCR clone in (C) and (D).

(C and D) 10^4 Thy1.1$^+$ CD4$^+$ TCR retrogenic (TCRrg) T cells were isolated from pooled SLOs of primary retrogenic mice and co-transferred with 10^6 RBC-lysed splenocytes from CD45$^{.1/.1}$ mice intravenously into *Tcrb*$^{-/-}$ secondary recipients (see STAR Methods). 3 weeks after transfer, the fate of transferred T cells was assessed in SLOs.

(C) Representative flow cytometric analysis of CD4$^+$ T cells isolated from indicated organs of secondary recipients that received RTSrg donor T cells. The top plots depict Thy1.1 versus CD45.1 expression by CD4$^+$ cells, whereas the middle and bottom plots depict Egr2 versus CD69 expression by donor Thy1.1$^+$ RTSrg or CD45.1$^+$ polyclonal CD4$^+$ T cells, respectively. The frequency of cells within the indicated gates is denoted.

(D) Summary plots of pooled data from (C), showing the frequency of Thy1.1$^+$ CD4$^+$ TCRrg T cells among total CD4$^+$ T cells (top) and the frequency of Thy1.1$^+$ CD4$^+$ TCRrg T cells expressing Egr2 and CD69 (bottom), isolated from indicated organs of secondary recipient mice. TCR clone names depicted refer to the 3rd–5th amino acids of the CDR3α sequence, underlined in (B). Mean is indicated. Dotted line denotes y axis = 1 (top) or y axis = 0 (bottom). n = 4–7 mice (RTS TCRrg), n = 2 mice (DPY TCRrg), n = 9 mice (PHI TCRrg), and n = 3 mice (KGN TCRrg).

Data are pooled from multiple independent experiments. aLN, axial lymph node; bLN, brachial lymph node; cLN, cervical lymph node; mLN, mesenteric lymph node; pLN, periaortic lymph node; Spl, spleen. One-way ANOVA with Tukey's post-test analysis, comparing all pairs in column (D; adjusted p values from Tukey's post-test are depicted). *p < 0.0.5, **p < 0.01, and ***p < 0.001. See also Tables S1 and S2.

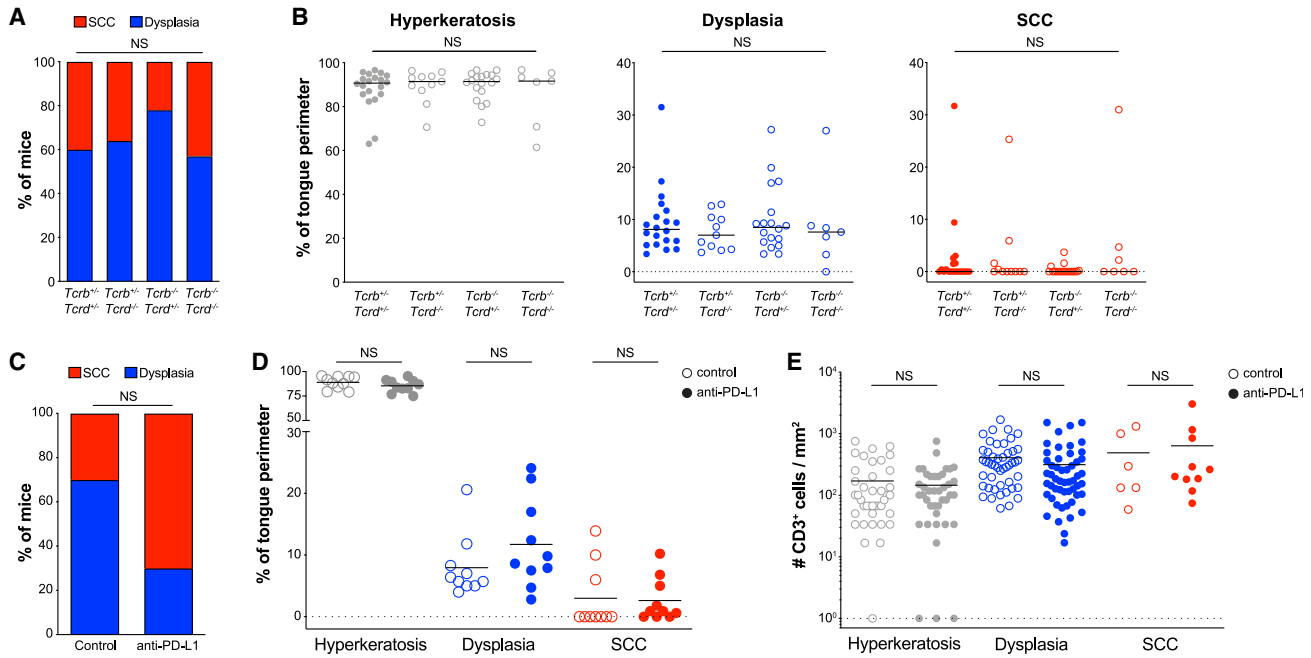

Figure 4. 4-NQO-induced lesions are not significantly impacted by the endogenous T cell response or treatment with checkpoint blockade monotherapies

(A and B) 6- to 8-week-old littermates of indicated genotype were exposed to 4-NQO drinking water for 20 weeks, tongues were subsequently excised, and histopathology was quantified as in Figure 2A. n = 20 mice (*Tcrb*$^{+/-}$ *Tcrd*$^{+/-}$), n = 11 mice (*Tcrb*$^{+/-}$ *Tcrd*$^{-/-}$), n = 18 mice (*Tcrb*$^{-/-}$ *Tcrd*$^{+/-}$), and n = 7 mice (*Tcrb*$^{-/-}$ *Tcrd*$^{-/-}$).

(A) Tumor incidence, where each mouse was scored once based on most severe histology grade observed. Summary plot of pooled data shows the percentage of mice scored as indicated histology grade. Each bar represents the cumulative data for mice of the indicated genotype.

(B) Tumor burden. Summary plots of pooled data show the percentage of tongue perimeter defined as hyperkeratosis (left plot), dysplasia (middle plot), or SCC (right plot). Each symbol represents an individual tongue from a single mouse of the indicated genotype. Median is indicated.

(C–E) 6- to 8-week-old female C57BL/6 mice were exposed to 4-NQO drinking water for 20 weeks. During the last 4 weeks of 4-NQO exposure, mice were treated intraperitoneally twice weekly with 100 μg anti-PD-L1 or isotype control monoclonal antibody. Tongues were excised at endpoint, and histopathology and IHC staining was performed and quantified as in Figures 2A and 2D. n = 10 mice per group.

(C) Tumor incidence, where each mouse was scored once based on most severe histology grade observed. Summary plot of pooled data shows the percentage of mice scored as indicated histology grade. Each bar represents the cumulative data for mice that received indicated antibody treatment.

(D) Tumor burden. Summary plot of pooled data shows the percentage of tongue perimeter defined as the indicated histology grade. Each symbol represents an individual tongue from a single mouse that received the indicated antibody treatment. Median is indicated.

(E) Summary plot of pooled data from CD3 IHC density analysis, showing the number of CD3$^+$ cells per mm^2 for each lesion. Each symbol represents an individual lesion. Median is indicated. n = 6–52 lesions from 10 mice per group.

Data are pooled from multiple independent experiments. Fisher's test (A and C); one-way ANOVA, comparing all pairs in column (B); two-tailed nonparametric Mann Whitney test (D and E). NS, not significant. See also Figure S2.

1 and 2), consistent with data presented in Figures 5B and 5C. However, in *Foxp3*$^{DTR/y}$ mice treated with DT plus anti-CD4 and anti-CD8 depleting antibodies, the impact of Treg cell ablation was abrogated, as OSCC incidence and burden remained at baseline (Figures 6B and 6C; compare data columns 2 and 4). In *Foxp3*$^{DTR/y}$ mice, DT plus anti-CD8 depleting antibody alone had no impact on OSCC incidence or burden compared to DT plus isotype control antibody (Figures S4B–S4D), demonstrating that effector CD4$^+$ Foxp3^{neg} T cells alone are sufficient to promote the emergence of OSCC following Treg cell ablation. Of note, analysis of *Foxp3*$^{WT/y}$ mice revealed that the depletion of all CD4$^+$ and CD8$^+$ T cells had no impact on the incidence of 4-NQO-induced lesions compared to isotype control antibody (Figures 6B and 6C; compare data columns 1 and 3), consistent with our findings in αβ T cell-deficient *Tcrb*$^{-/-}$ mice (Figures 4A and 4B). These collective findings demonstrate that the rapid emergence of OSCCs following late-stage Treg cell ablation is dependent on the presence of effector T cells, implying that the observed effects are dependent on a factor or factors produced by conventional T cells.

To better understand the mechanisms driving the rapid emergence of OSCCs following Treg cell ablation, we analyzed tissue sections for expression of the proliferation marker Ki-67. Density analysis revealed that, in lesions from non-Treg-depleted control mice, a substantial fraction of cells exhibiting a basal cell morphology stained positive for Ki-67 (Figure 6D). In lesions of Treg-cell-ablated mice, the percentage of cells of basal cell morphology staining positive for Ki-67 was comparable to controls (Figure 6E). In an effort to identify potential effector T cell-expressed factors that may contribute to the enhanced emergence of OSCC following Treg cell depletion, we analyzed T cell production of common effector cytokines by flow

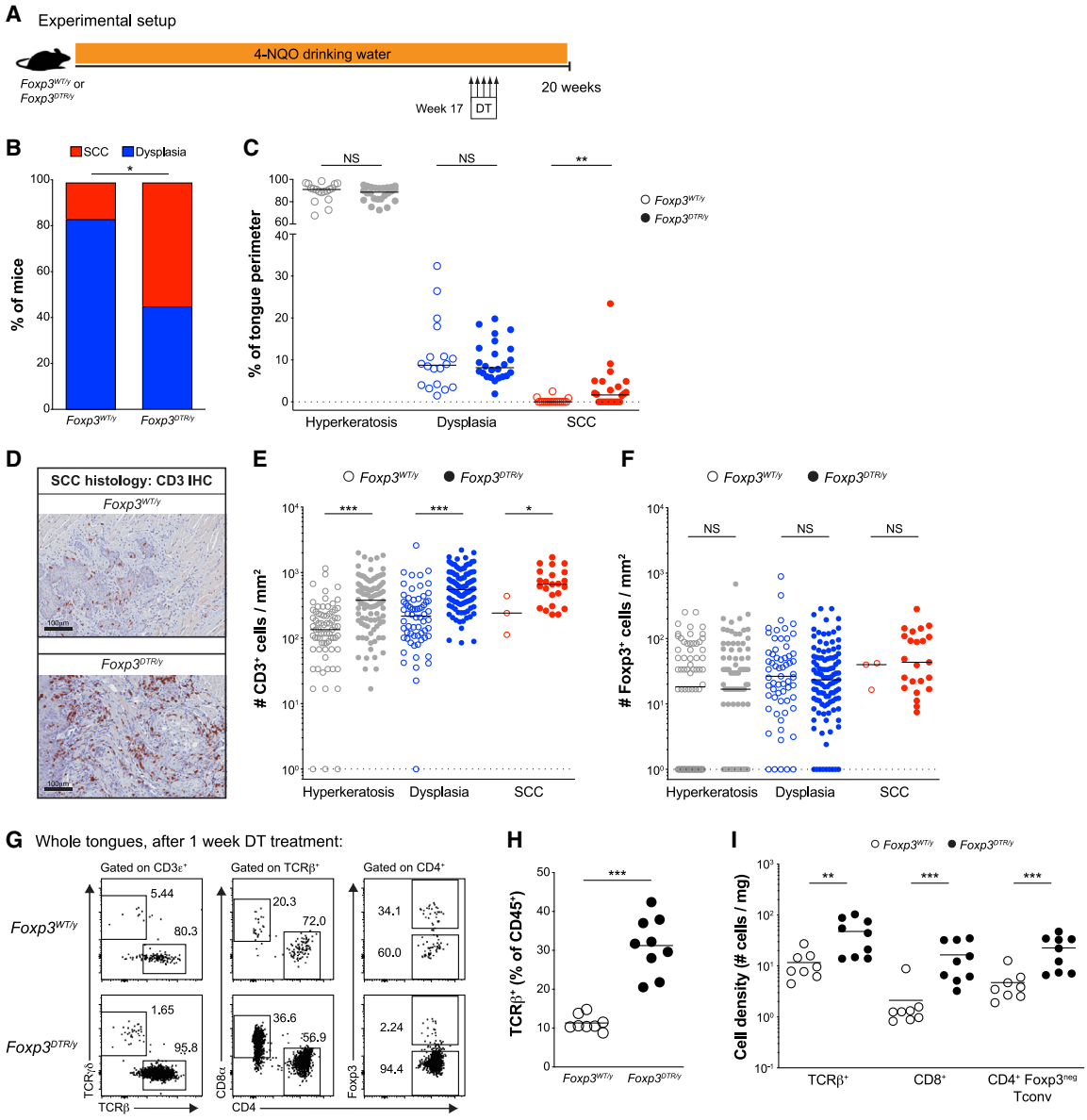

Figure 5. Late-stage Treg cell depletion enhances the emergence of invasive OSCC

(A) Experimental setup. 6- to 8-week-old *Foxp3*$^{WT/y}$ and *Foxp3*$^{DTR/y}$ littermates were exposed to 4-NQO drinking water for 20 weeks. During the 17th week of 4-NQO exposure, all mice were treated intraperitoneally every other day with diphtheria toxin (DT) for 1 week. Mice were sacrificed either 3 weeks later, at the 20-week endpoint, for histopathology analysis and IHC staining (B–F), or after the 1-week DT treatment, at 17-week endpoint, for flow cytometry analysis (G–I).

(B) Tumor incidence at 20-week endpoint, where each mouse was scored once based on most severe histology grade observed. Summary plot of pooled data shows the percentage of mice scored as indicated histology grade. Each bar represents the cumulative data for mice of the indicated genotype. n = 18 mice (*Foxp3*$^{WT/y}$); n = 24 mice (*Foxp3*$^{DTR/y}$).

(C) Tumor burden at 20-week endpoint. Summary plot of pooled data shows the percentage of tongue perimeter defined as the indicated histology grade. Each symbol represents an individual tongue from a single mouse of the indicated genotype. Median is indicated. n = 18 mice (*Foxp3*$^{WT/y}$); n = 24 mice (*Foxp3*$^{DTR/y}$).

(D) Representative CD3 IHC image of SCC region of tongue isolated from mice of the indicated genotype, at 20-week endpoint. Scale bar represents 100 μm.

(E) Summary plot of pooled data from CD3 IHC density analysis at 20-week endpoint, showing the number of CD3$^+$ cells per mm^2 for each lesion. Each symbol represents an individual lesion. Median is indicated. n = 3–110 lesions from 18–24 mice per group.

(F) Summary plot of pooled data from Foxp3 IHC density analysis at 20-week endpoint, showing the number of Foxp3$^+$ cells per mm^2 for each lesion. Each symbol represents an individual lesion. Median is indicated. n = 3–110 lesions from 18–24 mice per group.

(G) Representative flow cytometric analysis of T cells isolated from whole tongues of 4-NQO-treated mice of indicated genotype at 17-week endpoint, after 1 week of DT treatment. Left plots depict TCRβ versus TCRγδ expression by CD3$^+$ T cells, middle plots depict CD4 versus CD8α expression by αβT cells, and left plots depict CD4 versus Foxp3 expression by CD4$^+$ T cells. The frequency of cells within the indicated gates is denoted.

(legend continued on next page)

cytometry. These data revealed that Treg-cell-depleted mice harbored a greater fraction of tongue-associated CD3$^+$ T cells (primarily CD4$^+$ Foxp3^{neg} Tconv cells) that produced interferon γ (IFN-γ) (Figures 6F–6H). In contrast, the fraction of T cells producing interleukin-17A (IL-17A) and IL-4 was not elevated in Treg-cell-ablated mice (Figures 6F–6H). The increase in IFN-γ-producing effector T cells was associated with elevated tissue staining for phospho-STAT1, an intracellular readout of IFN-γ sensing (Figures 6I and 6J). Of note, cells of both lymphocyte and epithelial cell morphology stained positive for pSTAT1, suggesting that both immune cells and carcinoma cells were responding to cues in the local environment.

DISCUSSION

Our finding that late-stage Treg cell ablation enhances the incidence and burden of carcinogen-induced OSCCs suggests that strategies to promote *de novo* T cell infiltration in a subset of tumors that lack a substantial T cell infiltrate at baseline may yield unintended tumor-promoting effects. In this regard, Foxp3$^+$ Treg cells may sit at the fulcrum of such reactions, given their abundance within many human cancers (including OSCC), their potent regulatory functions, and the fact that Treg cells express high densities of many cell-surface receptors that are targeted by approved and emerging therapeutic antibodies. The potential for adverse consequences induced by immune-based therapy is also suggested by recent reports documenting patients with solid cancers, including those with HNSCC, that experience "hyper-progressive" disease following immunotherapy, characterized by accelerated tumor growth kinetics following therapy.[28,70–72] These collective findings highlight the importance of understanding the mechanisms driving accelerated disease following immunotherapy and delineating predictive biomarkers to identify patients who are at risk of such adverse events. The nature of the response to immune-based therapy is likely to be context dependent and impacted by a multitude of factors, including host and cancer genetics, the microbiota, the histological site of cancer origin, the stage of disease, and the local tissue environment. Moreover, due to heterogeneity in tumor biology and the composition of immune cells within the tumor environment, the response to immunotherapy may reflect a mixture of immune-mediated tumor control coupled with immune-mediated tumor promotion, depending on the state of distinct lesions at the time of therapy. Given our central finding that enhanced effector T cell infiltration induced by late-stage Treg cell ablation leads to increased incidence and burden of OSCCs, we anticipate that the addition of checkpoint blockade therapy would exacerbate disease even further. However, an alternate possibility is that the observed effects could be reversed by combining Treg cell depletion with agonist or blocking antibodies targeting common co-stimulatory or co-inhibitory axes, such as PD-1, OX40, 4-1BB, TIGIT, or GITR, thereby inducing regression of oral lesions.

Early studies using transplantable tumor models suggested that Treg cell depletion can promote immune-mediated tumor control.[65,66,68] In contrast, an expanding body of studies in autochthonous mouse cancer models reveals evidence that Treg cell ablation can have tumor-promoting effects, consistent with our current findings. In a mouse model of pancreatic cancer driven by oncogenic Kras activation, Zhang et al.[73] demonstrated that Treg cell ablation accelerated tumor progression and that this effect was abolished upon co-depletion of conventional CD4$^+$ T cells. In other studies, Martinez et al.[74] used an autochthonous model of polyoma middle-T oncogene-driven mammary carcinoma to demonstrate that Treg cell depletion at the pre-invasive ductal carcinoma *in situ* stage promoted progression to an early invasive carcinoma. Intriguingly, earlier research from the same group using orthotopic implantation of polyoma middle-T-driven tumors showed that Treg cell ablation in mice bearing advanced primary tumors deterred tumor outgrowth,[65] demonstrating that the impact of Treg cell ablation can be stage specific for a given cancer model. These collective findings, coupled with our current work, highlight the importance of utilizing animal models that accurately recapitulate the biology and pathogenesis of OSCC development and progression in humans, in which tumors arise *in situ* and progress from pre-neoplastic to invasive lesions.

At this time, the mechanisms driving the enhanced emergence of OSCC following late-stage Treg cell ablation remain incompletely defined. Our results to date suggest that a factor or factors expressed by effector T cells are required to drive rapid emergence of OSCC in this setting. It is possible that this phenomenon is due to indirect effects, such as local modulation of the inflammatory milieu, or due to direct interactions between T cells and tumor cells or their progenitors. It is also conceivable that other stromal cell types contribute to the observed reaction, including fibroblasts, endothelial cells, and non-transformed epithelial cells. Notably, previous work has demonstrated that tumor-associated conventional T cell populations can promote tumor progression in distinct contexts. This evidence includes the demonstration that IL-4-producing CD4$^+$ T cells promote metastasis in a murine model of mammary carcinoma[75] and the demonstration that CD4$^+$ T cells exhibiting a PD-1$^+$ T follicular helper-like phenotype are associated with diminished response to anti-PD-1 checkpoint blockade therapy.[76] Such findings are consistent with the notion that effector T cell subsets may promote cancer progression and that immune-based therapies have the potential to unleash undesirable tumor-promoting cascades in a subpopulation of patients. Our findings also provide a potential explanation for prognostic studies showing that high intratumoral Treg cell density is predictive of improved clinical outcome in OSCC and other HNSCCs.[24,26,27,35,40,42] In this scenario, intratumoral Treg cells may restrict tumor infiltration by tumor-promoting effector T cells, thereby contributing to the observed prognostic correlates. Moving forward, a key unresolved question in the

(H and I) Summary plots of pooled data from (G), showing the frequency of TCRβ$^+$ T cells among CD45$^+$ cells (H) or number of TCRβ$^+$, CD8$^+$, or CD4$^+$ Foxp3^{neg} T cells per mg of tissue (I), isolated from whole tongues of 4-NQO-treated mice of indicated genotype. Each symbol represents an individual mouse. Mean is indicated. n = 8 mice (*Foxp3*$^{WT/y}$); n = 9 mice (*Foxp3*$^{DTR/y}$).

Data are pooled from multiple independent experiments. Fisher's test (B); two-tailed nonparametric Mann Whitney test (C, E, F, H, and I). *$p < 0.0.5$, **$p < 0.01$, and ***$p < 0.001$. See also Figure S3.

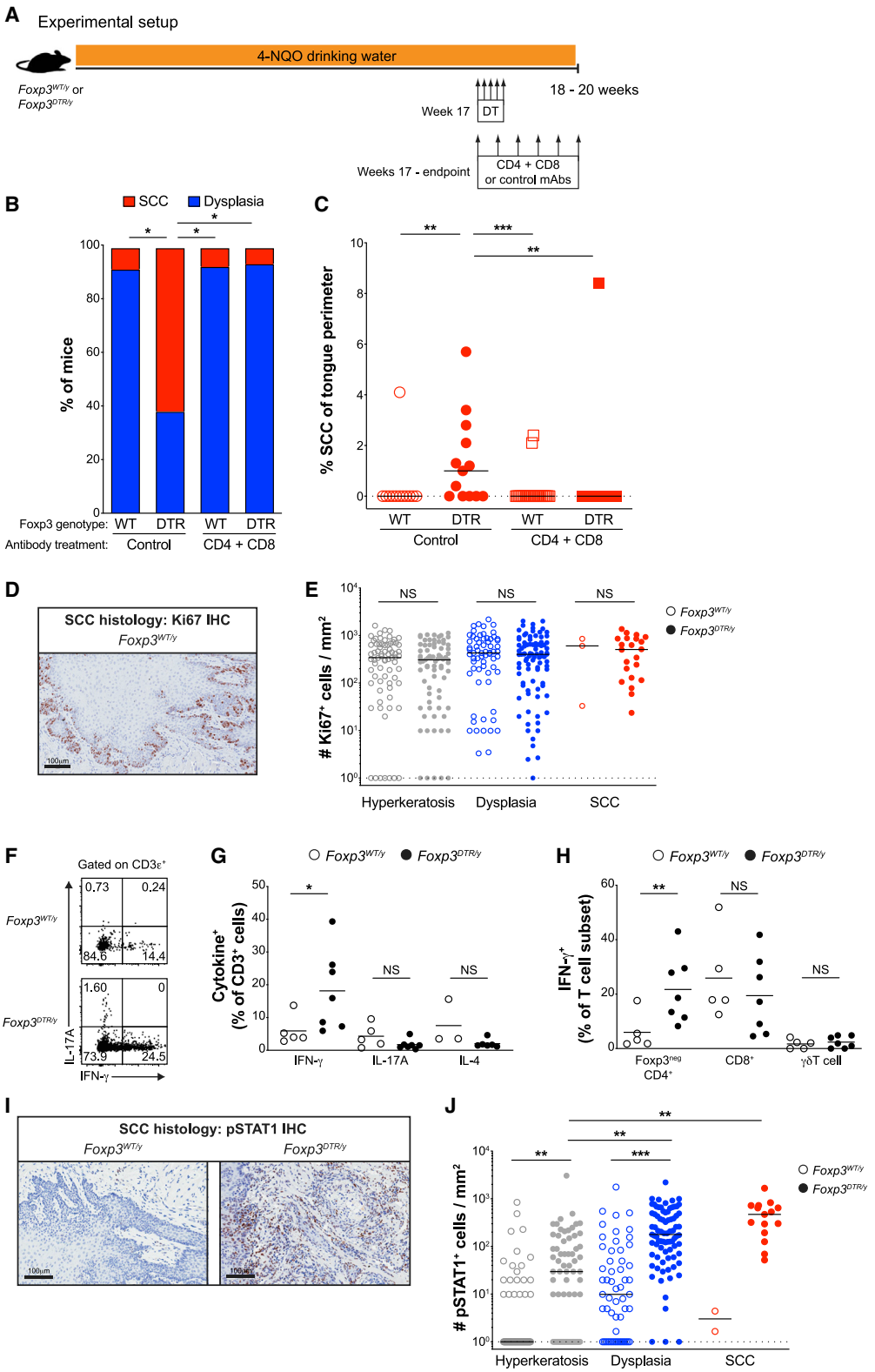

Figure 6. Increased incidence and burden of OSCC following late-stage Treg cell depletion is dependent on effector T cells

(A) Experimental setup for (B) and (C). 6- to 8-week-old *Foxp3*$^{DTR/y}$ and *Foxp3*$^{WT/y}$ littermates were exposed to 4-NQO drinking water for 20 weeks. During the 17th week of 4-NQO exposure, all mice were treated with DT for 1 week, as in Figure 5A. During weeks 17 through endpoint, mice were concomitantly injected

(legend continued on next page)

4-NQO-induced OSCC model is whether the enhanced emergence of carcinoma following Treg cell depletion is due to progression of dysplastic lesions to OSCC and/or rapid expansion of pre-existing OSCCs. In our studies, late-stage Treg cell depletion enhanced the emergence of OSCC, whereas earlier Treg cell ablation induced no measurable changes, suggesting that the observed effects are stage specific.

Lastly, our identification of polarized clusters of OSCC enriched for either $CD8^+$ T cells or $CD4^+$ Treg and conventional T cells demonstrates that the density of Treg cells does not correlate with that of $CD8^+$ T cells in many OSCCs and tumors of other solid cancer types. This finding implies that the factors driving intratumoral $CD4^+$ T cell abundance are likely distinct from those driving intratumoral $CD8^+$ T cell density in many tumors and indicates that the notion that Treg cell density largely "shadows" the density of tumor-infiltrating $CD8^+$ T cells[5,29,77] is not a universal principle applicable to all human cancers. This also suggests that, in some cases, categorization of tumors as "T cell inflamed" versus "T cell non-inflamed" lacks the resolution to articulate the immune landscape of a given tumor with respect to the relative representation of $CD8^+$ effector T cells, $CD4^+$ effector T cells, and $CD4^+$ $Foxp3^+$ Treg cells. Future work aimed at understanding the differential mechanisms driving $CD4^+$ versus $CD8^+$ T cell infiltration may reveal new approaches to selectively manipulate each T cell class within the tumor environment.

Limitations of study

The low and variable penetrance of 4-NQO-induced OSCCs is likely due to the stochastic nature of carcinogenesis and may be impacted by multiple factors, such as microbiota, diet, and extent of carcinogen exposure. Given that 4-NQO-induced lesions cannot be tracked longitudinally, it is not possible to distinguish whether the enhanced emergence of OSCC following late-stage Treg cell ablation is due to progression of premalignant lesions to malignant tumors, rapid expansion of pre-existing invasive carcinoma cells, or a combination of both. Our findings demonstrate that the enhanced emergence of OSCC following late-stage Treg cell depletion is dependent on effector T cells, but it remains unknown whether this is dependent on $CD4^+$ T cells, $CD8^+$ T cells, or both. Lastly, the T cell-expressed factors that drive exacerbation of OSCC remain undefined and could represent multiple pathways that are cooperative or redundant in nature. Future mechanistic studies are required to gain a better mechanistic understanding of these observations.

STAR★METHODS

Detailed methods are provided in the online version of this paper and include the following:

- KEY RESOURCES TABLE
- RESOURCE AVAILABILITY
  - Lead contact
  - Materials availability
  - Data and code availability
- EXPERIMENTAL MODEL AND SUBJECT DETAILS
  - Patient samples
  - Mice

intraperitoneally with 150 μg each of anti-CD4 + anti-CD8 depleting or isotype control antibodies (see STAR Methods). Tongues were excised at endpoint, and histopathology was quantified as in Figure 2A. n = 12 mice (B and C; $Foxp3^{WT/y}$, control antibodies), n = 13 mice (B and C; $Foxp3^{DTR/y}$, control antibodies), n = 26 mice (B and C; $Foxp3^{WT/y}$, anti-CD4 + anti-CD8 antibodies), and n = 16 mice (B and C; $Foxp3^{DTR/y}$, anti-CD4 + anti-CD8 antibodies).

(B) Tumor incidence, where each mouse was scored once based on most severe histology grade observed. Summary plot of pooled data, showing the percentage of mice scored as indicated histology grade. Each bar represents the cumulative data for mice of the indicated genotype and antibody treatment.

(C) Tumor burden. Summary plot of pooled data shows the percentage of tongue perimeter defined as SCC. Each symbol represents an individual tongue from a single mouse of the indicated genotype and antibody treatment. Median is indicated.

(D–J) Mice of indicated genotypes were exposed to 4-NQO drinking water for 20 weeks. During the 17^{th} week of 4-NQO exposure, all mice were treated with DT for 1 week, as in Figure 5A. Mice were sacrificed either 3 weeks later, at the 20-week endpoint, for IHC staining (D, E, I, and J), or after the 1-week DT treatment, at 17-week endpoint, for flow cytometry analysis (F–H).

(D) At the 20-week endpoint, tongues were excised and Ki-67 IHC staining was performed and quantified. Representative Ki-67 IHC image of SCC region of tongue isolated from a $Foxp3^{WT/y}$ mouse is shown. Scale bar represents 100 μm.

(E) Summary plot of pooled data from Ki-67 IHC density analysis, showing the number of $Ki\text{-}67^+$ cells per mm^2 for each lesion. Each symbol represents an individual lesion. Median is indicated. n = 3–89 lesions from 18 to 19 mice per group.

(F) Following 1-week DT treatment, at the 17-week endpoint, lymphocytes from 1–3 tongues were pooled, stimulated with phorbol 12-myristate 13-acetate (PMA) and ionomycin for 5 h, and analyzed by flow cytometry. Representative flow cytometric analysis of IFN-γ versus IL-17A expression by $CD3^+$ T cells isolated from tongues of mice of the indicated genotype is shown. The frequency of cells within the indicated gates is denoted.

(G) Summary plot of pooled data from (F), showing the frequency of $CD3^+$ T cell that are positive for IFN-γ, IL-17, or IL-4, isolated from pooled tongues of 4-NQO-treated mice of indicated genotype at the 17-week endpoint, after 1 week of DT treatment. Each symbol represents a pooled sample. Mean is indicated. n = 5 pooled samples from 11 mice ($Foxp3^{WT/y}$; IFN-γ and IL-17A), n = 7 pooled samples from 13 mice ($Foxp3^{DTR/y}$; IFN-γ and IL-17A), n = 3 pooled samples from 7 mice ($Foxp3^{WT/y}$; IL-4), and n = 6 pooled samples from 11 mice ($Foxp3^{DTR/y}$; IL-4).

(H) Summary plot of pooled data from (F), showing the frequency of IFN-γ^+ cells among $CD4^+$ $Foxp3^{neg}$ T cells, $CD8^+$ T cells, or γδT cells, isolated from pooled tongues of 4-NQO-treated mice of indicated genotype at the 17-week endpoint, after 1 week of DT treatment. Each symbol represents a pooled sample. Mean is indicated. n = 5 pooled samples from 11 mice ($Foxp3^{WT/y}$; IFN-γ and IL-17A), n = 7 pooled samples from 13 mice ($Foxp3^{DTR/y}$; IFN-γ and IL-17A), n = 3 pooled samples from 7 mice ($Foxp3^{WT/y}$; IL-4), and n = 6 pooled samples from 11 mice ($Foxp3^{DTR/y}$; IL-4).

(I) At the 20-week endpoint, tongues were excised and pSTAT1 IHC staining was performed and quantified. Representative pSTAT1 IHC image of SCC region of tongues isolated from mice of the indicated genotype is shown. Scale bar represents 100 μm.

(J) Summary plot of pooled data from pSTAT1 IHC density analysis, showing the number of $pSTAT1^+$ cells per mm^2 for each lesion. Each symbol represents an individual lesion. Median is indicated. n = 2–81 lesions from 16 to 17 mice per group.

Data are pooled from multiple independent experiments. mAb, monoclonal antibody. Fisher's test (B; adjusted p values from Bonferroni correction are depicted); one-way ANOVA with Dunn's post-test analysis, comparing all pairs in column (C and J; adjusted p values from Dunn's post-test are depicted); two-tailed nonparametric Mann Whitney test (E, G, and H). *$p < 0.0.5$, **$p < 0.01$, and ***$p < 0.001$. See also Figure S4.

SUPPLEMENTAL INFORMATION

Supplemental information can be found online at https://doi.org/10.1016/j.xcrm.2021.100399.

ACKNOWLEDGMENTS

We thank Christine Miller and Ryan Duncombe for technical assistance. We thank The University of Chicago CAT Facility (RRID: SCR_017760) for their assistance with flow cytometry. We thank The University of Chicago HTRC, especially Terri Li, for their assistance with histology and immunohistochemistry. This work was funded by The University of Chicago Comprehensive Cancer Center Pilot Project (to P.A.S.) and The University of Chicago Comprehensive Cancer Center Spotlight Award (to P.A.S. and E.I.). J.L.C. and M.T.W. were supported by T32-AI007090. E.I. was supported in part by R01-DE027809.

AUTHOR CONTRIBUTIONS

J.L.C. designed the study, performed experiments, interpreted data, and wrote the manuscript; M.K., A.Z., and I.V.O. performed transcriptome analysis of TCGA and CHGC datasets; M.T.W. performed experiments; and K.H. and M.W.L. provided expertise on tissue pathology. E.I. designed the study, interpreted data, and wrote the manuscript. P.A.S. designed the study, interpreted data, and wrote the manuscript. All authors contributed to discussion.

DECLARATION OF INTERESTS

M.K., A.Z., and I.V.O. are employees of Insilico Medicine Hong Kong, Ltd.

Received: February 15, 2021
Revised: July 8, 2021
Accepted: August 23, 2021
Published: September 14, 2021

REFERENCES

1. Chen, D.S., and Mellman, I. (2013). Oncology meets immunology: the cancer-immunity cycle. Immunity *39*, 1–10.
2. Chen, D.S., and Mellman, I. (2017). Elements of cancer immunity and the cancer-immune set point. Nature *541*, 321–330.
3. Thorsson, V., Gibbs, D.L., Brown, S.D., Wolf, D., Bortone, D.S., Ou Yang, T.-H., Porta-Pardo, E., Gao, G.F., Plaisier, C.L., Eddy, J.A., et al. (2018). The immune landscape of cancer. Immunity *48*, 812–830.e14.
4. Fridman, W.H., Zitvogel, L., Sautès-Fridman, C., and Kroemer, G. (2017). The immune contexture in cancer prognosis and treatment. Nat. Rev. Clin. Oncol. *14*, 717–734.
5. Gajewski, T.F., Corrales, L., Williams, J., Horton, B., Sivan, A., and Spranger, S. (2017). Cancer immunotherapy targets based on understanding the T cell-inflamed versus non-T cell-inflamed tumor microenvironment. Adv. Exp. Med. Biol. *1036*, 19–31.
6. Trujillo, J.A., Sweis, R.F., Bao, R., and Luke, J.J.T. (2018). T cell-inflamed versus non-T cell-inflamed tumors: a conceptual framework for cancer immunotherapy drug development and combination therapy selection. Cancer Immunol. Res. *6*, 990–1000.
7. Chao, J.L., and Savage, P.A. (2018). Unlocking the complexities of tumor-associated regulatory T cells. J. Immunol. *200*, 415–421.
8. Nishikawa, H., and Sakaguchi, S. (2014). Regulatory T cells in cancer immunotherapy. Curr. Opin. Immunol. *27*, 1–7.
9. Tanaka, A., and Sakaguchi, S. (2017). Regulatory T cells in cancer immunotherapy. Cell Res. *27*, 109–118.
10. deLeeuw, R.J., Kost, S.E., Kakal, J.A., and Nelson, B.H. (2012). The prognostic value of FoxP3+ tumor-infiltrating lymphocytes in cancer: a critical review of the literature. Clin. Cancer Res. *18*, 3022–3029.
11. Shang, B., Liu, Y., Jiang, S.J., and Liu, Y. (2015). Prognostic value of tumor-infiltrating FoxP3+ regulatory T cells in cancers: a systematic review and meta-analysis. Sci. Rep. *5*, 15179.
12. Cipolletta, D., Feuerer, M., Li, A., Kamei, N., Lee, J., Shoelson, S.E., Benoist, C., and Mathis, D. (2012). PPAR-γ is a major driver of the accumulation and phenotype of adipose tissue Treg cells. Nature *486*, 549–553.
13. Feuerer, M., Herrero, L., Cipolletta, D., Naaz, A., Wong, J., Nayer, A., Lee, J., Goldfine, A.B., Benoist, C., Shoelson, S., and Mathis, D. (2009). Lean, but not obese, fat is enriched for a unique population of regulatory T cells that affect metabolic parameters. Nat. Med. *15*, 930–939.
14. Burzyn, D., Kuswanto, W., Kolodin, D., Shadrach, J.L., Cerletti, M., Jang, Y., Sefik, E., Tan, T.G., Wagers, A.J., Benoist, C., and Mathis, D. (2013). A special population of regulatory T cells potentiates muscle repair. Cell *155*, 1282–1295.
15. Arpaia, N., Green, J.A., Moltedo, B., Arvey, A., Hemmers, S., Yuan, S., Treuting, P.M., and Rudensky, A.Y. (2015). A distinct function of regulatory T cells in tissue protection. Cell *162*, 1078–1089.
16. Ali, N., Zirak, B., Rodriguez, R.S., Pauli, M.L., Truong, H.-A., Lai, K., Ahn, R., Corbin, K., Lowe, M.M., Scharschmidt, T.C., et al. (2017). Regulatory T cells in skin facilitate epithelial stem cell differentiation. Cell *169*, 1119–1129.e11.
17. De Simone, M., Arrigoni, A., Rossetti, G., Gruarin, P., Ranzani, V., Politano, C., Bonnal, R.J.P., Provasi, E., Sarnicola, M.L., Panzeri, I., et al. (2016). Transcriptional landscape of human tissue lymphocytes unveils uniqueness of tumor-infiltrating T regulatory cells. Immunity *45*, 1135–1147.
18. Plitas, G., Konopacki, C., Wu, K., Bos, P.D., Morrow, M., Putintseva, E.V., Chudakov, D.M., and Rudensky, A.Y. (2016). Regulatory T cells exhibit distinct features in human breast cancer. Immunity *45*, 1122–1134.
19. Tirosh, I., Izar, B., Prakadan, S.M., Wadsworth, M.H., 2nd, Treacy, D., Trombetta, J.J., Rotem, A., Rodman, C., Lian, C., Murphy, G., et al. (2016). Dissecting the multicellular ecosystem of metastatic melanoma by single-cell RNA-seq. Science *352*, 189–196.
20. Togashi, Y., Shitara, K., and Nishikawa, H. (2019). Regulatory T cells in cancer immunosuppression - implications for anticancer therapy. Nat. Rev. Clin. Oncol. *16*, 356–371.
21. Zheng, C., Zheng, L., Yoo, J.-K., Guo, H., Zhang, Y., Guo, X., Kang, B., Hu, R., Huang, J.Y., Zhang, Q., et al. (2017). Landscape of infiltrating T cells in liver cancer revealed by single-cell sequencing. Cell *169*, 1342–1356.e16.
22. Alexandrov, L.B., Nik-Zainal, S., Wedge, D.C., Aparicio, S.A.J.R., Behjati, S., Biankin, A.V., Bignell, G.R., Bolli, N., Borg, A., Børresen-Dale, A.L., et al.; Australian Pancreatic Cancer Genome Initiative; ICGC Breast Cancer Consortium; ICGC MMML-Seq Consortium; ICGC PedBrain (2013).

Signatures of mutational processes in human cancer. Nature *500*, 415–421.

23. Alexandrov, L.B., Kim, J., Haradhvala, N.J., Huang, M.N., Tian Ng, A.W., Wu, Y., Boot, A., Covington, K.R., Gordenin, D.A., Bergstrom, E.N., et al.; PCAWG Mutational Signatures Working Group; PCAWG Consortium (2020). The repertoire of mutational signatures in human cancer. Nature *578*, 94–101.

24. Mandal, R., Şenbabaoğlu, Y., Desrichard, A., Havel, J.J., Dalin, M.G., Riaz, N., Lee, K.W., Ganly, I., Hakimi, A.A., Chan, T.A., and Morris, L.G. (2016). The head and neck cancer immune landscape and its immunotherapeutic implications. JCI Insight *1*, e89829.

25. Seiwert, T.Y., Burtness, B., Mehra, R., Weiss, J., Berger, R., Eder, J.P., Heath, K., McClanahan, T., Lunceford, J., Gause, C., et al. (2016). Safety and clinical activity of pembrolizumab for treatment of recurrent or metastatic squamous cell carcinoma of the head and neck (KEYNOTE-012): an open-label, multicentre, phase 1b trial. Lancet Oncol. *17*, 956–965.

26. Echarti, A., Hecht, M., Büttner-Herold, M., Haderlein, M., Hartmann, A., Fietkau, R., and Distel, L. (2019). CD8+ and regulatory T cells differentiate tumor immune phenotypes and predict survival in locally advanced head and neck cancer. Cancers (Basel) *11*, E1398.

27. Seminerio, I., Descamps, G., Dupont, S., de Marrez, L., Laigle, J.-A., Lechien, J.R., Kindt, N., Journe, F., and Saussez, S. (2019). Infiltration of FoxP3+ regulatory T cells is a strong and independent prognostic factor in head and neck squamous cell carcinoma. Cancers (Basel) *11*, E227.

28. Saâda-Bouzid, E., Defaucheux, C., Karabajakian, A., Coloma, V.P., Servois, V., Paoletti, X., Even, C., Fayette, J., Guigay, J., Loirat, D., et al. (2017). Hyperprogression during anti-PD-1/PD-L1 therapy in patients with recurrent and/or metastatic head and neck squamous cell carcinoma. Ann. Oncol. *28*, 1605–1611.

29. Roychoudhuri, R., Eil, R.L., and Restifo, N.P. (2015). The interplay of effector and regulatory T cells in cancer. Curr. Opin. Immunol. *33*, 101–111.

30. Puram, S.V., Tirosh, I., Parikh, A.S., Patel, A.P., Yizhak, K., Gillespie, S., Rodman, C., Luo, C.L., Mroz, E.A., Emerick, K.S., et al. (2017). Single-cell transcriptomic analysis of primary and metastatic tumor ecosystems in head and neck cancer. Cell *171*, 1611–1624.e24.

31. Keck, M.K., Zuo, Z., Khattri, A., Stricker, T.P., Brown, C.D., Imanguli, M., Rieke, D., Endhardt, K., Fang, P., Brägelmann, J., et al. (2015). Integrative analysis of head and neck cancer identifies two biologically distinct HPV and three non-HPV subtypes. Clin. Cancer Res. *21*, 870–881.

32. Makarev, E., Schubert, A.D., Kanherkar, R.R., London, N., Teka, M., Ozerov, I., Lezhnina, K., Bedi, A., Ravi, R., Mehra, R., et al. (2017). *In silico* analysis of pathways activation landscape in oral squamous cell carcinoma and oral leukoplakia. Cell Death Discov. *3*, 17022.

33. Ozerov, I.V., Lezhnina, K.V., Izumchenko, E., Artemov, A.V., Medintsev, S., Vanhaelen, Q., Aliper, A., Vijg, J., Osipov, A.N., Labat, I., et al. (2016). *In silico* pathway activation network decomposition analysis (iPANDA) as a method for biomarker development. Nat. Commun. *7*, 13427.

34. Saloura, V., Izumchenko, E., Zuo, Z., Bao, R., Korzinkin, M., Ozerov, I., Zhavoronkov, A., Sidransky, D., Bedi, A., Hoque, M.O., et al. (2019). Immune profiles in primary squamous cell carcinoma of the head and neck. Oral Oncol. *96*, 77–88.

35. Boxberg, M., Leising, L., Steiger, K., Jesinghaus, M., Alkhamas, A., Mielke, M., Pfarr, N., Götz, C., Wolff, K.D., Weichert, W., et al. (2019). Composition and clinical impact of the immunologic tumor microenvironment in oral squamous cell carcinoma. J. Immunol. *202*, 278–291.

36. Chatzopoulos, K., Sotiriou, S., Collins, A.R., Kartsidis, P., Schmitt, A.C., Chen, X., Khazaie, K., Hinni, M.L., Ramsower, C.A., Zarka, M.A., et al. (2021). Transcriptomic and immunophenotypic characterization of tumor immune microenvironment in squamous cell carcinoma of the oral tongue. Head Neck Pathol. *15*, 509–522.

37. Cillo, A.R., Kürten, C.H.L., Tabib, T., Qi, Z., Onkar, S., Wang, T., Liu, A., Duvvuri, U., Kim, S., Soose, R.J., et al. (2020). Immune landscape of viral- and carcinogen-driven head and neck cancer. Immunity *52*, 183–199.e9.

38. Liu, X., Chen, J., Lu, W., Zeng, Z., Li, J., Jiang, X., Gao, Y., Gong, Y., Wu, Q., and Xie, C. (2020). Systematic profiling of immune risk model to predict survival and immunotherapy response in head and neck squamous cell carcinoma. Front. Genet. *11*, 576566.

39. Aran, D., Hu, Z., and Butte, A.J. (2017). xCell: digitally portraying the tissue cellular heterogeneity landscape. Genome Biol. *18*, 220.

40. Koike, K., Dehari, H., Ogi, K., Shimizu, S., Nishiyama, K., Sonoda, T., Sasaki, T., Sasaya, T., Tsuchihashi, K., Hasegawa, T., et al. (2020). Prognostic value of FoxP3 and CTLA-4 expression in patients with oral squamous cell carcinoma. PLoS ONE *15*, e0237465.

41. Salama, P., Phillips, M., Grieu, F., Morris, M., Zeps, N., Joseph, D., Platell, C., and Iacopetta, B. (2009). Tumor-infiltrating FOXP3+ T regulatory cells show strong prognostic significance in colorectal cancer. J. Clin. Oncol. *27*, 186–192.

42. Yao, Y., Yan, Z., Lian, S., Wei, L., Zhou, C., Feng, D., Zhang, Y., Yang, J., Li, M., and Chen, Y. (2020). Prognostic value of novel immune-related genomic biomarkers identified in head and neck squamous cell carcinoma. J. Immunother. Cancer *8*, e000444.

43. Hasina, R., Martin, L.E., Kasza, K., Jones, C.L., Jalil, A., and Lingen, M.W. (2009). ABT-510 is an effective chemopreventive agent in the mouse 4-nitroquinoline 1-oxide model of oral carcinogenesis. Cancer Prev. Res. (Phila.) *2*, 385–393.

44. Ishida, K., Tomita, H., Nakashima, T., Hirata, A., Tanaka, T., Shibata, T., and Hara, A. (2017). Current mouse models of oral squamous cell carcinoma: genetic and chemically induced models. Oral Oncol. *73*, 16–20.

45. Kanojia, D., and Vaidya, M.M. (2006). 4-nitroquinoline-1-oxide induced experimental oral carcinogenesis. Oral Oncol. *42*, 655–667.

46. Tang, X.-H., Knudsen, B., Bemis, D., Tickoo, S., and Gudas, L.J. (2004). Oral cavity and esophageal carcinogenesis modeled in carcinogen-treated mice. Clin. Cancer Res. *10*, 301–313.

47. Vitale-Cross, L., Czerninski, R., Amornphimoltham, P., Patel, V., Molinolo, A.A., and Gutkind, J.S. (2009). Chemical carcinogenesis models for evaluating molecular-targeted prevention and treatment of oral cancer. Cancer Prev. Res. (Phila.) *2*, 419–422.

48. Czerninski, R., Amornphimoltham, P., Patel, V., Molinolo, A.A., and Gutkind, J.S. (2009). Targeting mammalian target of rapamycin by rapamycin prevents tumor progression in an oral-specific chemical carcinogenesis model. Cancer Prev. Res. (Phila.) *2*, 27–36.

49. Sequeira, I., Rashid, M., Tomás, I.M., Williams, M.J., Graham, T.A., Adams, D.J., Vigilante, A., and Watt, F.M. (2020). Genomic landscape and clonal architecture of mouse oral squamous cell carcinomas dictate tumour ecology. Nat. Commun. *11*, 5671.

50. Wang, Z., Wu, V.H., Allevato, M.M., Gilardi, M., He, Y., Luis Callejas-Valera, J., Vitale-Cross, L., Martin, D., Amornphimoltham, P., Mcdermott, J., et al. (2019). Syngeneic animal models of tobacco-associated oral cancer reveal the activity of in situ anti-CTLA-4. Nat. Commun. *10*, 5546.

51. Park, J.-Y., Chung, H., DiPalma, D.T., Tai, X., and Park, J.-H. (2018). Immune quiescence in the oral mucosa is maintained by a uniquely large population of highly activated Foxp3$^+$ regulatory T cells. Mucosal Immunol. *11*, 1092–1102.

52. Wu, R., Zhang, D., Zanvit, P., Jin, W., Wang, H., and Chen, W. (2020). Identification and regulation of TCR$\alpha\beta^+$CD8$\alpha\alpha^+$ intraepithelial lymphocytes in murine oral mucosa. Front. Immunol. *11*, 1702.

53. Blatner, N.R., Mulcahy, M.F., Dennis, K.L., Scholtens, D., Bentrem, D.J., Phillips, J.D., Ham, S., Sandall, B.P., Khan, M.W., Mahvi, D.M., et al. (2012). Expression of RORγt marks a pathogenic regulatory T cell subset in human colon cancer. Sci. Transl. Med. *4*, 164ra159.

54. Gounaris, E., Blatner, N.R., Dennis, K., Magnusson, F., Gurish, M.F., Strom, T.B., Beckhove, P., Gounari, F., and Khazaie, K. (2009). T-regulatory cells

shift from a protective anti-inflammatory to a cancer-promoting proinflammatory phenotype in polyposis. Cancer Res. *69*, 5490–5497.

55. Kachler, K., Holzinger, C., Trufa, D.I., Sirbu, H., and Finotto, S. (2018). The role of Foxp3 and Tbet co-expressing Treg cells in lung carcinoma. OncoImmunology *7*, e1456612.
56. Meinicke, H., Bremser, A., Brack, M., Akeus, P., Pearson, C., Bullers, S., Hoffmeyer, K., Stemmler, M.P., Quiding-Järbrink, M., and Izcue, A. (2017). Tumour-associated changes in intestinal epithelial cells cause local accumulation of KLRG1^{+} GATA3^{+} regulatory T cells in mice. Immunology *152*, 74–88.
57. Dash, P., McClaren, J.L., Oguin, T.H., 3rd, Rothwell, W., Todd, B., Morris, M.Y., Becksfort, J., Reynolds, C., Brown, S.A., Doherty, P.C., and Thomas, P.G. (2011). Paired analysis of TCRα and TCRβ chains at the single-cell level in mice. J. Clin. Invest. *121*, 288–295.
58. Malchow, S., Leventhal, D.S., Nishi, S., Fischer, B.I., Shen, L., Paner, G.P., Amit, A.S., Kang, C., Geddes, J.E., Allison, J.P., et al. (2013). Aire-dependent thymic development of tumor-associated regulatory T cells. Science *339*, 1219–1224.
59. Malchow, S., Leventhal, D.S., Lee, V., Nishi, S., Socci, N.D., and Savage, P.A. (2016). Aire enforces immune tolerance by directing autoreactive T cells into the regulatory T cell lineage. Immunity *44*, 1102–1113.
60. Miller, C.H., Klawon, D.E.J., Zeng, S., Lee, V., Socci, N.D., and Savage, P.A. (2020). Eomes identifies thymic precursors of self-specific memory-phenotype CD8^{+} T cells. Nat. Immunol. *21*, 567–577.
61. McDonald, B.D., Bunker, J.J., Ishizuka, I.E., Jabri, B., and Bendelac, A. (2014). Elevated T cell receptor signaling identifies a thymic precursor to the TCRαβ(+)CD4(-)CD8β(-) intraepithelial lymphocyte lineage. Immunity *41*, 219–229.
62. Leemans, C.R., Snijders, P.J.F., and Brakenhoff, R.H. (2018). The molecular landscape of head and neck cancer. Nat. Rev. Cancer *18*, 269–282.
63. Schumacher, T.N., and Schreiber, R.D. (2015). Neoantigens in cancer immunotherapy. Science *348*, 69–74.
64. Ayers, M., Lunceford, J., Nebozhyn, M., Murphy, E., Loboda, A., Kaufman, D.R., Albright, A., Cheng, J.D., Kang, S.P., Shankaran, V., et al. (2017). IFN-γ-related mRNA profile predicts clinical response to PD-1 blockade. J. Clin. Invest. *127*, 2930–2940.
65. Bos, P.D., Plitas, G., Rudra, D., Lee, S.Y., and Rudensky, A.Y. (2013). Transient regulatory T cell ablation deters oncogene-driven breast cancer and enhances radiotherapy. J. Exp. Med. *210*, 2435–2466.
66. Jang, J.-E., Hajdu, C.H., Liot, C., Miller, G., Dustin, M.L., and Bar-Sagi, D. (2017). Crosstalk between regulatory T cells and tumor-associated dendritic cells negates anti-tumor immunity in pancreatic cancer. Cell Rep. *20*, 558–571.
67. Pastille, E., Bardini, K., Fleissner, D., Adamczyk, A., Frede, A., Wadwa, M., von Smolinski, D., Kasper, S., Sparwasser, T., Gruber, A.D., et al. (2014). Transient ablation of regulatory T cells improves antitumor immunity in colitis-associated colon cancer. Cancer Res. *74*, 4258–4269.
68. Teng, M.W.L., Ngiow, S.F., von Scheidt, B., McLaughlin, N., Sparwasser, T., and Smyth, M.J. (2010). Conditional regulatory T-cell depletion releases adaptive immunity preventing carcinogenesis and suppressing established tumor growth. Cancer Res. *70*, 7800–7809.
69. Kim, J.M., Rasmussen, J.P., and Rudensky, A.Y. (2007). Regulatory T cells prevent catastrophic autoimmunity throughout the lifespan of mice. Nat. Immunol. *8*, 191–197.
70. Champiat, S., Dercle, L., Ammari, S., Massard, C., Hollebecque, A., Postel-Vinay, S., Chaput, N., Eggermont, A., Marabelle, A., Soria, J.-C., et al. (2017). Hyperprogressive disease is a new pattern of progression in cancer patients treated by anti-PD-1/PD-L1. Clin. Cancer Res. *23*, 1920–1928.
71. Kato, S., Goodman, A., Walavalkar, V., Barkauskas, D.A., Sharabi, A., and Kurzrock, R. (2017). Hyperprogressors after immunotherapy: analysis of genomic alterations associated with accelerated growth rate. Clin. Cancer Res. *23*, 4242–4250.
72. Kim, J.Y., Lee, K.H., Kang, J., Borcoman, E., Saada-Bouzid, E., Kronbichler, A., Hong, S.H., de Rezende, L.F.M., Ogino, S., Keum, N., et al. (2019). Hyperprogressive disease during anti-PD-1 (PDCD1) / PD-L1 (CD274) therapy: a systematic review and meta-analysis. Cancers (Basel) *11*, E1699.
73. Zhang, Y., Lazarus, J., Steele, N.G., Yan, W., Lee, H.-J., Nwosu, Z.C., Halbrook, C.J., Menjivar, R.E., Kemp, S.B., Sirihorachai, V.R., et al. (2020). Regulatory T-cell depletion alters the tumor microenvironment and accelerates pancreatic carcinogenesis. Cancer Discov. *10*, 422–439.
74. Martinez, L.M., Robila, V., Clark, N.M., Du, W., Idowu, M.O., Rutkowski, M.R., and Bos, P.D. (2019). Regulatory T cells control the switch from *in situ* to invasive breast cancer. Front. Immunol. *10*, 1942.
75. DeNardo, D.G., Barreto, J.B., Andreu, P., Vasquez, L., Tawfik, D., Kolhatkar, N., and Coussens, L.M. (2009). CD4(+) T cells regulate pulmonary metastasis of mammary carcinomas by enhancing protumor properties of macrophages. Cancer Cell *16*, 91–102.
76. Zappasodi, R., Budhu, S., Hellmann, M.D., Postow, M.A., Senbabaoglu, Y., Manne, S., Gasmi, B., Liu, C., Zhong, H., Li, Y., et al. (2018). Non-conventional inhibitory CD4^{+}Foxp3^{-}PD-1^{hi} T cells as a biomarker of immune checkpoint blockade activity. Cancer Cell *33*, 1017–1032.e7.
77. Spranger, S., Spaapen, R.M., Zha, Y., Williams, J., Meng, Y., Ha, T.T., and Gajewski, T.F. (2013). Up-regulation of PD-L1, IDO, and T(regs) in the melanoma tumor microenvironment is driven by CD8(+) T cells. Sci. Transl. Med. *5*, 200ra116.
78. Leonard, J.D., Gilmore, D.C., Dileepan, T., Nawrocka, W.I., Chao, J.L., Schoenbach, M.H., Jenkins, M.K., Adams, E.J., and Savage, P.A. (2017). Identification of natural regulatory T cell epitopes reveals convergence on a dominant autoantigen. Immunity *47*, 107–117.e8.
79. Cancer Genome Atlas Network (2015). Comprehensive genomic characterization of head and neck squamous cell carcinomas. Nature *517*, 576–582.
80. R Development Core Team (2021). R: the R project for statistical computing. https://www.r-project.org/.
81. Schindelin, J., Arganda-Carreras, I., Frise, E., Kaynig, V., Longair, M., Pietzsch, T., Preibisch, S., Rueden, C., Saalfeld, S., Schmid, B., et al. (2012). Fiji: an open-source platform for biological-image analysis. Nat. Methods *9*, 676–682.
82. Schelker, M., Feau, S., Du, J., Ranu, N., Klipp, E., MacBeath, G., Schoeberl, B., and Raue, A. (2017). Estimation of immune cell content in tumour tissue using single-cell RNA-seq data. Nat. Commun. *8*, 2032.
83. Moon, J.J., Chu, H.H., Pepper, M., McSorley, S.J., Jameson, S.C., Kedl, R.M., and Jenkins, M.K. (2007). Naive CD4(+) T cell frequency varies for different epitopes and predicts repertoire diversity and response magnitude. Immunity *27*, 203–213.

STAR★METHODS

KEY RESOURCES TABLE

REAGENT or RESOURCE	SOURCE	IDENTIFIER
Antibodies		
Anti-CD3 antibody, Rabbit monoclonal, clone SP162	Sigma-Aldrich	Cat# SAB5500057
FOXP3 Monoclonal Antibody, clone FJK-16 s	eBioscience	Cat# 14-5773-82, RRID: AB_467576
Rabbit Anti-Stat1, phospho (Tyr701) Monoclonal Antibody, clone 58D6, unconjugated	Cell Signaling	Cat# 9167, RRID:AB_561284
Rabbit Anti-Human Ki67 (Ki-67) Monoclonal Antibody, Unconjugated, Clone SP6	Thermo Fisher	Cat# RM-9106-S, RRID: AB_149707
anti-mouse/human CD45R/B220 antibody, clone RA3-6B2, APC conjugated	BioLegend	Cat# 103211, RRID:AB_312996
anti-mouse/human CD45R/B220 antibody, clone RA3-6B2, FITC conjugated	BioLegend	Cat# 103205, RRID:AB_312990
anti-mouse/human CD45R/B220 antibody, clone RA3-6B2, Pacific Blue conjugated	BioLegend	Cat# 103230, RRID:AB_492877
anti-mouse/human CD45R/B220 antibody, clone RA3-6B2, PE/Cy7 conjugated	BioLegend	Cat# 103221, RRID:AB_313004
anti-mouse/human CD11b antibody, clone M1/70, BV605 conjugated	BioLegend	Cat# 101237, RRID:AB_11126744
anti-mouse/human CD11b antibody, clone M1/70, Pacific Blue conjugated	BioLegend	Cat# 101223, RRID:AB_755985
anti-mouse CD11c antibody, clone N418, APC conjugated	BioLegend	Cat# 117310, RRID:AB_313779
anti-mouse CD11c antibody, clone N418, Pacific Blue conjugated	BioLegend	Cat# 117321, RRID:AB_755987
anti-mouse CD127 (IL-7Ralpha) antibody, clone A7R34, PE/Cy7 conjugated	BioLegend	Cat# 135013, RRID:AB_1937266
anti-mouse CD25 antibody, clone PC61, APC conjugated	BioLegend	Cat# 102011, RRID:AB_312860
anti-mouse CD3 antibody, clone 17A2, Alexa Fluor 700 conjugated	BioLegend	Cat# 100216, RRID:AB_493697
anti-mouse CD3 antibody, clone 17A2, APC/Cy7 conjugated	BioLegend	Cat# 100221, RRID:AB_2057374
anti-mouse CD3 antibody, clone 17A2, PE/Cy7 conjugated	BioLegend	Cat# 100219, RRID:AB_1732068
anti-mouse CD4 antibody, clone RM4-5, BV605 conjugated	BioLegend	Cat# 100547, RRID:AB_11125962
CD4 Monoclonal Antibody, clone RM4-5, eFluor 450 conjugated	eBioscience	Cat# 48-0042-82, RRID:AB_1272194
anti-mouse CD4 antibody, clone GK1.5, PerCP/Cy5.5 conjugated	BioLegend	Cat# 100434, RRID:AB_893324
anti-mouse/human CD44 antibody, clone IM7, APC/Cy7 conjugated	BioLegend	Cat# 103028, RRID:AB_830785
anti-mouse/human CD44 antibody, clone IM7, FITC conjugated	BioLegend	Cat# 103006, RRID:AB_312957
anti-mouse CD45.1 antibody, clone A20, Alexa Fluor 700 conjugated	BioLegend	Cat# 110724, RRID:AB_493733

(*Continued on next page*)

Continued

REAGENT or RESOURCE	SOURCE	IDENTIFIER
anti-mouse CD45.2 antibody, clone 104, APC/Cy7 conjugated	BioLegend	Cat# 109823, RRID:AB_830788
anti-mouse CD45.2 antibody, clone 104, BV711 conjugated	BioLegend	Cat# 109847, RRID:AB_2616859
anti-mouse CD62L antibody, clone MEL-14, PE conjugate	BioLegend	Cat# 104408, RRID:AB_313095
anti-mouse CD69 antibody, clone H1.2F3, PE/Cy7 conjugated	BioLegend	Cat# 104512, RRID:AB_493564
anti-mouse CD8a antibody, clone 53-6.7, APC/Cy7 conjugated	BioLegend	Cat# 100714, RRID:AB_312753
anti-mouse CD8a antibody, clone 53-6.7, PE/Cy7 conjugated	BioLegend	Cat# 100721, RRID:AB_312760
anti-mouse CD8a antibody, clone 53-6.7, PerCP/Cy5.5 conjugated	BioLegend	Cat# 100733, RRID:AB_2075239
anti-mouse CD8b (Ly-3) antibody, clone YTS156.7.7, Alexa Fluor 700 conjugated	BioLegend	Cat# 126618, RRID:AB_2563949
anti-mouse CD8b (Ly-3) antibody, clone YTS156.7.7, APC/Cy7 conjugated	BioLegend	Cat# 126619, RRID:AB_2563950
anti-mouse CD8b (Ly-3) antibody, clone YTS156.7.7, PerCP/Cy5.5 conjugated	BioLegend	Cat# 126609, RRID:AB_961304
EGR2 Monoclonal Antibody, clone erongr2, APC conjugated	eBioscience	Cat# 17-6691-80, RRID:AB_11150966
anti-mouse F4/80 antibody, clone BM8, Pacific Blue conjugated	BioLegend	Cat# 123124, RRID:AB_893475
FOXP3 Monoclonal Antibody, clone FJK-16 s, APC conjugated	eBioscience	Cat# 17-5773-82, RRID:AB_469457
FOXP3 Monoclonal Antibody, clone FJK-16 s, eFluor 450 conjugated	eBioscience	Cat# 48-5773-82, RRID:AB_1518812
FOXP3 Monoclonal Antibody, clone FJK-16 s, FITC conjugated	eBioscience	Cat# 11-5773-82, RRID:AB_465243
FOXP3 Monoclonal Antibody, clone FJK-16 s, PE conjugated	eBioscience	Cat# 12-5773-82, RRID:AB_465936
FOXP3 Monoclonal Antibody, clone FJK-16 s, PE/Cy7 conjugated	eBioscience	Cat# 25-5773-82, RRID:AB_891552
Gata-3 Monoclonal Antibody, clone TWAJ, PE conjugated	eBioscience	Cat# 12-9966-41, RRID:AB_1963601
Gata-3 Monoclonal Antibody, clone TWAJ, PerCP-eFluor 710 conjugated	eBioscience	Cat# 46-9966-42, RRID:AB_10804487
anti-mouse Ly-6G/Ly-6C (Gr-1) antibody, clone RB6-8C5, APC/Cy7 conjugated	BioLegend	Cat# 108424, RRID:AB_2137485
anti-mouse I-A/I-E antibody, clone M5/ 114.15.2, Pacific Blue conjugated	BioLegend	Cat# 107620, RRID:AB_493527
anti-mouse IFN-γ antibody, clone XMG1.2, APC conjugated	BD Biosciences	Cat# 562018, RRID:AB_10896992
IL-17A Monoclonal Antibody, clone eBio17B7, PE conjugated	eBioscience	Cat# 12-7177-81, RRID:AB_763582
anti-mouse IL-4 antibody, clone 11B11, BV421 conjugated	BioLegend	Cat# 504119, RRID:AB_10896945
Rat Anti-Mouse IL-4 Antibody, clone 11B11, BV650 conjugated	BD Biosciences	Cat# 564004, RRID:AB_2687569
anti-mouse Ly-6C antibody, clone HK1.4, PE conjugated	BioLegend	Cat# 128007, RRID:AB_1186133

(*Continued on next page*)

Continued

REAGENT or RESOURCE	SOURCE	IDENTIFIER
anti-mouse Ly-6G antibody, clone 1A8, FITC conjugated	BioLegend	Cat# 127606, RRID:AB_1236494
Mouse Anti-Mouse RORγt, clone Q31-378, BV786 conjugated	BD Biosciences	Cat# 564723, RRID:AB_2738916
anti-T-bet antibody, clone 4B10, BV421 conjugated	BioLegend	Cat# 644816, RRID:AB_10959653
anti-mouse TCR beta chain antibody, clone H57-597, BV510 conjugated	BioLegend	Cat# 109234, RRID:AB_2562350
anti-mouse TCR beta chain antibody, clone H57-597, PE conjugated	BioLegend	Cat# 109207, RRID:AB_313430
anti-mouse TCR beta chain antibody, clone H57-597, PE/Cy7 conjugated	BioLegend	Cat# 109221, RRID:AB_893627
anti-mouse TCR gamma/delta antibody, clone GL3, APC conjugated	BioLegend	Cat# 118116, RRID:AB_1731813
anti-mouse TCR gamma/delta antibody, clone GL3, PE/Cy7 conjugated	BioLegend	Cat# 118123, RRID:AB_11203530
anti-rat CD90/mouse CD90.1 (Thy-1.1) antibody, clone OX-7, PE conjugated	BioLegend	Cat# 202524, RRID:AB_1595524
anti-mouse CD90.2 (Thy1.2) antibody, clone 53-2.1, FITC conjugated	BioLegend	Cat# 140304, RRID:AB_10642812
anti-mouse TNF-alpha antibody, clone MP6-XT22, BV421 conjugated	BioLegend	Cat# 506327, RRID:AB_10900823
2W1S/I-A^b tetramer, APC conjugated	Laboratory of P.A.S.	Leonard et al.[78]
2W1S/I-A^b tetramer, PE conjugated	Laboratory of P.A.S.	Leonard et al.[78]
InVivoPlus anti-mouse CTLA-4 (CD152) antibody, clone 9D9	BioXCell	Cat# BE0164, RRID:AB_10949609
InVivoPlus anti-mouse PD-1 (CD279) antibody, clone RMP1-14	BioXCell	Cat# BE0146, RRID:AB_10949053
InVivoPlus anti-mouse PD-L1 (B7-H1) antibody, clone 10F.9G2	BioXCell	Cat# BE0101, RRID:AB_10949073
InVivoPlus anti-mouse CD4 antibody, clone GK1.5	BioXCell	Cat# BE0003-1, RRID:AB_1107636
InVivoPlus anti-mouse CD8α antibody, clone 2.43	BioXCell	Cat# BE0061, RRID:AB_1125541
InVivoPlus mouse IgG2b isotype control antibody, clone MPC-11	BioXCell	Cat# BE0086, RRID:AB_1107791
InVivoPlus rat IgG2a isotype control antibody, clone 2A3	BioXCell	Cat# BE0089, RRID:AB_1107769
InVivoPlus rat IgG2b isotype control antibody, clone LTF-2	BioXCell	Cat# BE0090, RRID:AB_1107780
Bacterial and virus strains		
E. coli DH5α	New England Biolabs	Cat# C2987H
Chemicals, peptides, and recombinant proteins		
4-Nitroquinoline *N*-oxide	Sigma-Aldrich	Cat# N8141
Dimethyl sulfoxide	Sigma-Aldrich	Cat# D4540
Propylene Glycol	Fisher Scientific	Cat# P355-1
Formalin solution, neutral buffered, 10%	Sigma-Aldrich	Cat# HT501128
Diphtheria Toxin from *Corynebacterium diphtheriae*	Sigma-Aldrich	Cat# D0564
Complete Freund's Adjuvant (CFA)	InvivoGen	Cat# vac-cfa-10
Custom 2W1S peptide (EAWGALANWAVDSA), > 98% pure	GenScript	N/A

(*Continued on next page*)

Continued

REAGENT or RESOURCE	SOURCE	IDENTIFIER
Liberase TL Research Grade	Roche	Cat# 5401020001
DNase I, grade II, from bovine pancreas	Roche	Cat# 10104159001
Phorbol 12-myristate 13-acetate (PMA)	Sigma-Aldrich	Cat# 79346
Ionomycin calcium salt from *Streptomyces conglobatus*	Sigma-Aldrich	Cat# I0634
Monensin Solution (1000X)	eBioscience	Cat# 00-4505-51
5-Fluorouracil	APP Pharmaceuticals	Cat# 101710
Recombinant Mouse M-CSF (carrier free)	BioLegend	Cat# 576406
Recombinant Mouse IL-3 (carrier free)	BioLegend	Cat# 575504
Recombinant Mouse IL-6 (carrier free)	BioLegend	Cat# 575706
Polybrene Infection / Transfection Reagent	EMD Millipore	Cat# TR-1003-G
Critical commercial assays		
CD4 $^{+}$ T Cell Isolation Kit, mouse	Miltenyi Biotec	Cat# 130-104-454
EasySep PE Positive Selection Kit	Stem Cell Technologies	Cat# 18557
EasySep APC Positive Selection Kit	Stem Cell Technologies	Cat# 18453
Foxp3 / Transcription Factor Staining Buffer Set	eBioscience	Cat# 00-5523-00
Maxima First Strand cDNA Synthesis Kit for RT-qPCR	Thermo Scientific	Cat# K1641
DreamTaq Green PCR Master Mix (2X)	Thermo Scientific	Cat# K1081
Deposited data		
TCRα sequence dataset	This paper	Table S2
TCRα catalogs	Malchow et al.[59]	https://linkinghub.elsevier.com/retrieve/pii/S1074761316300474
TCGA-HNSCC dataset	Cancer Genome Atlas Network[79]	http://www.nature.com/articles/nature14129
CHGC dataset	Keck et al.[31]	GEO: GSE40774
TCGA datasets (kidney renal clear cell carcinoma, liver hepatocellular carcinoma, lung adenocarcinoma, melanoma)	https://www.cancer.gov/about-nci/organization/ccg/research/structural-genomics/tcga	N/A
Experimental models: Cell lines		
Plat-E Retroviral Packaging Cell Line	Cell Biolabs	Cat# RV-101
Experimental models: Organisms/strains		
Mouse: B6: C57BL/6J	Jackson Laboratories	JAX: 000664
Mouse: Foxp3-DTR: B6.129(Cg)-*Foxp3*$^{tm3(DTR/GFP)Ayr}$/J	Jackson Laboratories	JAX: 016958
Mouse: *Tcrb*$^{-/-}$ *x Tcrd*$^{-/-}$: B6.129P2-*Tcrb*^{tm1Mom} *Tcrd*^{tm1mom}/J	Jackson Laboratories	JAX: 002122
Mouse: *Rag1*$^{-/-}$ (B6.129S7-*Rag1*^{tm1Mom}/J)	Jackson Laboratories	JAX: 002216
Mouse: *Tcra*$^{-/-}$ (B6.129S2-*Tcra*^{tm1Mom}/J)	Jackson Laboratories	JAX: 002116
Mouse: CD4-Cre (B6.Cg-Tg(Cd4-cre)1Cwi/BfluJ)	Jackson Laboratories	JAX: 022071
Mouse: *Foxp3*^{GFP} (B6.Cg-*Foxp3*^{tm2Tch}/J)	Jackson Laboratories	JAX: 006772
Mouse: TCRβtg: transgenic mouse expressing (TRBV26)- ASSLGSSYEQY TCRβ chain	Laboratory of P.A.S.	Malchow et al.[58]
Recombinant DNA		
I-A ^{b} alpha chain in pRMHa3	Laboratory of E.J. Adams	Leonard et al.[78]
I-A ^{b} beta chain (2W1S peptide) in pRMHa3	Laboratory of E.J. Adams	Leonard et al.[78]
pMGflThy1.1	Laboratory of A. Bendelac	McDonald et al.[61]

(*Continued on next page*)

Continued

REAGENT or RESOURCE	SOURCE	IDENTIFIER
Software and algorithms		
Prism (v9.0.0)	GraphPad	https://www.graphpad.com:443/
FlowJo v10.7.1	BD Biosciences	https://www.flowjo.com
R v4.0.2	R Core Team[80]	https://www.r-project.org/
Fiji	Schindelin et al.[81]	https://fiji.sc/
iPANDA	Ozerov et al.[33]	N/A
xCell R package (version 1.12)	Aran et al.[39]	https://github.com/dviraran/xCell
Aperio ImageScope	Leica	https://www.leicabiosystems.com/
Other		
Aperio ScanScope XT	Leica	N/A
LSR Fortessa	BD Biosciences	N/A
FACSAria	BD Biosciences	N/A

RESOURCE AVAILABILITY

Lead contact

Further information and requests for resources and reagents should be directed to and will be fulfilled by the Lead Contact, Peter A. Savage (psavage@bsd.uchicago.edu).

Materials availability

This study generated 4 retroviral vectors encoding the CDR3α sequence for RTS, DPY, PHI, or KGN TCRs, available upon request.

Data and code availability

Source data for patient datasets used for Figures 1 and S1 is available at http://www.nature.com/articles/nature14129 and https://www.cancer.gov/about-nci/organization/ccg/research/structural-genomics/tcga . The single-cell TCRα sequence data generated in this study are available in Table S2. Source TCRα sequence data and analysis used for $CD4^+$ $Foxp3^+$ Treg and $CD4^+$ $Foxp3^{neg}$ Tconv catalogs in Figures 3A and 3B is available at https://linkinghub.elsevier.com/retrieve/pii/S1074761316300474.
Source code used for analysis for Figures 1 and S1 is available at http://www.nature.com/articles/ncomms13427 and https://doi.org/10.5281/zenodo.1004662. Original code used for IHC density analysis is available in supplemental information Methods S1.
Any additional information required to reanalyze the data reported in this paper is available from the lead contact upon request.

EXPERIMENTAL MODEL AND SUBJECT DETAILS

Patient samples

Two OSCC transcriptomic data cohorts of patients with locoregionally advanced disease were utilized, The Cancer Genome Atlas–Head-and-Neck Squamous Cell Carcinoma (TCGA-HNSC) dataset (http://www.nature.com/articles/nature14129)[79] restricted to HPV-negative OSCC data (n = 259) and the Chicago HNC (head and neck cancer) Genomics Cohort (CHGC) (GEO: GSE40774)[31] restricted to HPV-negative OSCC data (n = 78). Only tumors of oral cavity were included to the analysis, while other anatomical sites (larynx, hypopharynx, oropharynx and tonsil) were excluded. Transcriptomic data of patients with kidney renal clear cell carcinoma (n = 535), liver hepatocellular carcinoma (n = 374), lung adenocarcinoma (n = 527), and melanoma (n = 471) are based upon data generated by the TCGA Research Network: https://www.cancer.gov/about-nci/organization/ccg/research/structural-genomics/tcga.

Mice

The following mice were purchased from the Jackson Laboratory, and bred and maintained at the University of Chicago under specific pathogen-free conditions: B6 (C57BL/6J) mice, Foxp3-DTR (B6.129(Cg)-*Foxp3*$^{tm3(DTR/GFP)Ayr}$/J) mice, *Tcrb* $^{-/-}$ *x Tcrd* $^{-/-}$ (B6.129P2-*Tcrb*^{tm1Mom} *Tcrd*^{tm1mom}/J) mice, *Rag1*$^{-/-}$ (B6.129S7-*Rag1*^{tm1Mom}/J) mice, *Tcra*$^{-/-}$ (B6.129S2-*Tcra*^{tm1Mom}/J) mice, CD4-Cre (B6.Cg-Tg(Cd4-cre)1Cwi/BfluJ) mice, and *Foxp3*^{GFP} (B6.Cg-*Foxp3*^{tm2Tch}/J) mice. "TCRβtg" mice expressing a fixed TCRβ chain of sequence TRBV26-ASSLGSSYEQY were generated as described previously[58]. All mice were generated on a pure B6 background or were fully backcrossed to the B6 background. All mice were bred and maintained under specific pathogen-free conditions, and all experiments were conducted in accordance with the animal care and use regulations of the Institutional Animal Care and Use Committee (IACUC) at the University of Chicago (protocol #72053). Mice for experiments were age-matched, cage-mates, and littermates

when possible, and assigned to experimental groups randomly and based on genotype, when appropriate. Both male and female mice were used for experiments, as appropriate.

Cell Lines and Bacteria

Drosophila S2 cells were used for recombinant production of I-A^b; cells were transfected according to the *Drosophila* Expression System manual (Thermo Fisher) in Schneider's *Drosophila* medium supplemented with 10% FBS, 1X Pen/Strep (100 U/mL penicillin, 0.1 mg/mL streptomycin), and 20 μg/mL gentamicin, and maintained in stationary cultures at 27°C. S2 transfectants were selected with 25 μg/mL Blasticidin, and stable lines were expanded for expression in Express Five SFM supplemented with 25 μg/mL Blasticidin, 1X Pen/Strep, and 20 μg/mL gentamicin, in suspension culture shaking at 120 rpm and 27°C. Plat-E cells (Cell Biolabs) were used for retroviral packaging of TCRα-containing pMGflThy1.1 plasmid; cells were grown in Dulbecco's Modified Eagle's Medium 14 (GIBCO) supplemented with 10% FBS, 1X Pen/Strep, 10 μg/mL Blasticidin, and 1 μg/mL Puromycin and maintained in stationary cultures at 37°C. Plat-E transfectants were cultured in the absence of Blasticidin and Puromycin. *E. coli* DH5α (New England Biolabs) was used for cloning and propagation of TCRα-containing pMGflThy1.1 plasmid.

METHOD DETAILS

Deconvolution of bulk transcriptomic profiles

Pre-processed gene expression data was loaded into the version of iPANDA algorithm[33,34] with disabled gene grouping and topological weights. The 'off' state of topology coefficients means that they are equal to 1 for all genes during the calculation. The 'off' state for the gene grouping means that all the genes are treated as individual genes. Deconvolution was performed using a collection of differentially expressed genes that facilitate annotation of the four T cell subtypes as naive-like, regulatory, cytotoxic, and exhausted[30], and the estimated proportion of each subtype was calculated for each sample[82]. Activation signs for all the genes was obtained from Puram et al.[30] and iPANDA algorithm was used for the dimension reduction in gene expression data prior to the clustering and data visualization[34]. In order to validate the results, another deconvolution algorithm, xCell[39], was used. The "xCell" R package (version 1.12) was used to generate immune estimates for the xCell method[39]. A general immune estimation score for cases from TCGA cohort was already generated by xCell and is publicly available. For comparison purposes, only cell types which could be detected by both iPANDA and xCell were used for validation.

Administration of 4-NQO

6-8 week old mice were administered 4-NQO in their drinking water for a continuous period of 20 weeks, unless otherwise noted. For stock solution, 4-NQO powder (Sigma) was dissolved in DMSO at a 50 mg/mL concentration and stored at −20°C until use. Stock solution was dissolved in propylene glycol (Sigma) and added to drinking water for a final concentration of 100 μg/mL 4-NQO in 0.6% propylene glycol. 4-NQO drinking water was replaced weekly.

Tongue tissue histology and immunohistochemistry

Tongues were isolated and fixed in 10% buffered formalin (Sigma) for 24-48 h then longitudinally bisected and embedded in paraffin. Consecutive 5 μm sections were stained with hematoxylin and eosin (H&E) for blinded histopathological analysis or processed for immunohistochemical detection of CD3, Foxp3, pSTAT1, or Ki-67 antigens using anti-CD3 (clone SP162, Sigma-Aldrich), anti-Foxp3 (clone FJK-16 s, Invitrogen), anti-pSTAT1 (Tyr701) (clone 58D6, Cell Signaling), anti-Ki-67 (clone SP6, Thermo Scientific) antibodies, respectively. Slides were scanned at 40X using the Aperio ScanScope XT and viewed and analyzed on the accompanying software ImageScope. Tissue processing, staining, and digital scanning was performed by the Human Tissue Resource Center at University of Chicago. To analyze histopathology incidence, each H&E slide was scored once based on the most severe grade present, using established criteria[43]: normal epithelium, hyperkeratosis, dysplasia, or invasive squamous cell carcinoma. To analyze histopathology burden, the epithelial perimeter of each tongue was outlined, and each region was scored as normal epithelium, hyperkeratosis, dysplasia, or invasive squamous cell carcinoma. In this way, each histological grade defined a certain percentage of the total perimeter of the sample. For immunohistochemistry quantification, images were captured at 40X and positive cells were counted in an automated fashion in ImageJ[81] using the a custom macro code available in Methods S1.

Treg cell depletion with diphtheria toxin (DT)

For late-stage Treg cell depletion, mice were treated with 1 μg DT (Sigma) via intraperitoneal (i.p.) injections on days 0, 1, 3, 5, and 7 during the 17th week of 4-NQO exposure. In some experiments, Treg cells were depleted in a periodic and transient manner, in which mice were treated with 1 μg DT on two consecutive days during the 9th, 12th, 15th, and 18th week of 4-NQO exposure.

Monoclonal antibody treatment

For immunotherapy treatment, mice were treated with 100 μg of the following monoclonal antibodies via i.p. injections twice weekly, starting during the 17th week of 4-NQO exposure: anti-CTLA-4 (clone 9D9), anti-PD-1 (clone RMP1-14), anti-PD-L1 (clone 10F.9G2), or control (clones MPC11, 2A3, or LTF-2). For T cell depletion, mice were treated with 150 μg of the following monoclonal antibodies

via i.p. injections twice during the first week, following by weekly treatments, starting during the 17th week of 4-NQO exposure: anti-CD4 (clone GK1.5), anti-CD8 (clone 2.43), or control (clone LTF-2). All antibodies for *in vivo* use were purchased from BioXCell.

Immunization with peptide plus CFA

Mice were given a single subcutaneous (s.c.) injection on the flank of 100 μg of 2W1S peptide (GenScript) in 100 μL of CFA emulsion (InvivoGen) after 18 weeks of 4-NQO exposure. CFA emulsion consisted of a 1:1 ratio peptide:CFA. Mice were analyzed 2 weeks later.

Cell isolation, flow cytometry, and fluorescence-activated cell sorting

Cells from secondary lymphoid organs were isolated into single cell suspension in RPMI-1640 media supplemented with 10% FBS and 1% penicillin/streptomycin using a 70 μm filter. To harvest tongue-infiltrating lymphocytes, tongues were excised and injected and digested with 5 mM EDTA in RPMI-1640 for 15 min at 37°C, followed by digestion with Liberase TL (10 mg/mL, Roche) and DNase (20 mg/mL, Roche) in RPMI-1640 for 30 min at 37°C. Digested organ tissues were mechanically disrupted with frosted microscope slides and viable lymphocytes were enriched using Histopaque 1119 (Sigma). Cells were stained with conjugated antibodies specific for the following proteins (clone name in parentheses): B220 (RA3-6B2), CD11b (M1/70), CD11c (N418), CD127 (A7R34), CD25 (PC61.5), CD3ε (17A2), CD4 (RM4-5 or GK1.5), CD44 (IM7), CD45.1 (A20), CD45.2 (104), CD62L (MEL-14), CD69 (H1.2F3), CD8α (53-6.7), CD8β (YTS156.7.7), Egr2 (erongr2), F4/80 (BM8), Foxp3 (FJK-16 s), Gata3 (TWAJ), Gr-1 (RB6-8C5), I-A/I-E (M5/114.15.2), IFN-γ (XMG1.2), IL-17A (eBio17B7), IL-4 (11B11), Ly6C (HK1.4), Ly6G (1A8), RORγt (Q31-378), T-bet (4B10), TCRβ (H57-597), TCRγδ (GL3), Thy1.1 (OX-7), Thy1.2 (53-2.1), TNFα (MP6-XT22). Cells were stained for 20 min at 4°C in staining buffer (PBS with 2% FCS, 0.1 NaN_3, 5% normal rat serum, 5% normal mouse serum, 5% normal rabbit serum (all sera from The Jackson Laboratory), and 10 μg/mL 2.4G2 antibody). Overnight intracellular staining for Foxp3, T-bet, Gata3, RORγt, IFN-γ, IL-17A, IL-4, and TNFα was performed using the Foxp3 Transcription Factor Staining Buffer Set (eBioscience). In experiments involving tetramer staining, cells were stained as previously described[78]. Briefly, cells were stained with PE- and APC-labeled 2W1S/I-A^b tetramers at a final concentration of 10 nM for 1 h at room temperature, followed by enrichment using the EasySep™ PE Positive Selection Kit (StemCell Technologies). The resulting bound fraction was stained for surface and intracellular proteins as described above. Flow cytometry was performed on an LSR Fortessa (BD Biosciences) and data were analyzed using FlowJo software (TreeStar). Fluorescence-activated cell sorting (FACS) was preformed using a FACSAria (BD Biosciences).

In vitro T cell stimulation

Lymphocytes from tongues were isolated into single cell suspension as described above and plated into 96-well U-bottom plates, pooling 1-3 mice per well. Cells were stimulated with PMA (50 ng/mL, Sigma) and Ionomycin (500 ng/mL, Sigma) for 5 h. Monensin (2uM, eBioscience) was added to the culture during the last 4 h of incubation. T cells were then stained to assess cytokine profile, as described above.

TCR sequence analysis

Foxp3^{GFP} x TCRβtg mice were treated with 4-NQO drinking water for 8 weeks, then supplied normal drinking water for an additional 24 weeks. Lymphocytes from whole tongues were isolated into single cell suspension as described above, and Foxp3-GFP$^+$ Treg cells were single-cell sorted into catch solution (sterile H_20 with TRIS (pH 8.0, Ambio) and RNase inhibitor (Promega)) in 96 well U-bottom plates and processed for TCRα sequencing analysis, as described in Dash et al.[57] with modifications. Briefly, cDNA synthesis was performed directly from single cells using Maxima First Strand cDNA Synthesis Kit (Thermo Scientific) per manufacturer's instructions with minor modifications. The cDNA synthesis used 6 μL of reaction mix consisting of 3 μL 5X Reaction Mix, 0.5 μL Maxima Enzyme Mix, and 1.25% IGEPAL (Sigma). This was added to the 10 μL single cell-containing solution and incubated at 25°C for 10 min, 50°C for 50 min, and 85°C for 5 min. Following reverse transcription, multiplex PCR was performed to amplify the CDR3α transcripts in a 20 μL reaction mix containing 2 μL cDNA and DreamTaq Green Master Mix (Thermo Scientific). The first round of PCR used a mixture of 23 TRAV forward and 1 TRAC reverse primers. The PCR conditions were 94°C for 5 min followed by 45 cycles of 94°C for 30 s, 56°C for 30 s, and 72°C for 1 min, with a final extension at 72°C for 8 min. The second round of PCR used the product from the first round of PCR as template and a mixture internal 23 TRAV forward and 1 TRAC reverse primers. The PCR conditions were similar to the first round but with 50 cycles. The nested PCR product was purified using EXOSap-IT (Applied Biosystems) per the manufacturer's instructions, and sequenced using the internal TRAC reverse primer. TCRα sequences were analyzed and assigned using the international ImMunoGeneTics information system (IMGT) database (http://www.imgt.org).

Retrovirus production, infection, and generation of TCR retrogenic (TCRrg) mice

TCRrg mice were generated as previously described[60,61,78]. In brief, the *Tcra* sequence that encodes a TCRα chain of interest was cloned into a modified retroviral construct. Plat-E cells were used to generate retrovirus. *Tcra*$^{-/-}$ CD4-Cre$^+$ TCRβtg$^+$ mice were injected with 5-fluorouracil (APP Pharmaceuticals) three days prior to bone marrow harvest. Bone marrow cells were then cultured for two days in X-Vivo 10 media (Lonza) supplemented with 15% FCS, 1% penicillin/streptomycin, 100 ng/mL mouse SCF, 10 ng/mL mouse IL-3, and 20 ng/mL mouse IL-6 (BioLegend). Cells were infected with retrovirus by spinfection in the presence of 6 μg/mL polybrene (EMD Millipore) and cultured for an additional 24 h. All spinfected cells were then mixed with 5 × 10^6 freshly harvested

bone marrow "filler" cells from *Rag1*$^{-/-}$ mice and injected intravenously (i.v.) into lethally irradiated (800 rad) CD45$^{.1/.1}$ B6.SJL recipient mice to produce "primary TCRrg" mice. For "secondary TCRrg" mice, CD4^{+} T cells were FACS-purified from primary TCRrg mice following CD4 MACS enrichment (Miltenyi Biotech) and 10^4 Thy1.1^{+} CD4^{+} T cells were transferred i.v. with 10^6 freshly harvested "filler" RBC-lysed splenocytes from CD45$^{.1/.1}$ mice into *Tcrb*$^{-/-}$ hosts. "Secondary TCRrg" mice were analyzed three weeks later.

2W1S/I-A^{b} Tetramer Production

2W1S/I-A^{b} tetramers bearing the 2W1S peptide (EAWGALANWAVDSA) were produced using methods similar to those described previously[78,83]. I-A^{b} was expressed in *Drosophila* S2 cells, using separate plasmids to encode the alpha and beta chains, as described previously (Leonard and Gilmore et al., 2017).[78,83] Constructs were co-transfected into *Drosophila* S2 cells together with a plasmid encoding the BirA biotin ligase. Protein expression was induced with the addition of 0.8 mM $CuSO_4$, in the presence of 2 μg/mL biotin (Sigma-Aldrich). Biotinylated I-A^{b} protein was purified from culture supernatant by nickel affinity chromatography with His Bind Ni-IDA resin (EMD Millipore) and by avidin affinity chromatography with Pierce Monomeric Avidin UltraLink Resin (Thermo Fisher). Tetramers were formed by mixing biotinylated I-A^{b} with streptavidin-APC (Prozyme PJ27S) or streptavidin-PE (Prozyme PJRS34) at a slight molar excess of I-A^{b} to biotin binding sites. Saturation of the streptavidin conjugate was verified by non-reducing SDS-PAGE without boiling samples.

I-A^{b} Alpha Chain

The extracellular domain of the I-A^{b} alpha chain (underlined) was fused at its N terminus to a secretion signal sequence (boundary denoted by "/"), and at its C terminus to an acidic leucine zipper, and a recognition sequence for the BirA biotin ligase.

MPCSRALILGVLALTTMLSLCGG/EDDIEADHVGTYGISVYQSPGDIGQYTFEFDGDELFYVDLDKKETVWMLPEFGQLASFDPQGGL
QNIAVVKHNLGVLTKRSNSTPATNEAPQATVFPKSPVLLGQPNTLICFVDNIFPPVINITWLRNSKSVADGVYETSFFVNRDYSFHKLSYLT
FIPSDDDIYDCKVEHWGLEEPVLKHWEPEIPAPMSELTETGGGGSTTAPSAQLEKELQALEKENAQLEWELQALEKELAQGGSGGSGL
NDIFEAQKIEWHE.

I-A^{b} Beta Chain with 2W1S Peptide

The extracellular domain of the I-A^{b} beta chain (underlined) was fused at its N terminus to a secretion signal sequence (boundary denoted by "/"), the 2W1S peptide (in bold) and a linker sequence, and at its C terminus to a basic leucine zipper and a 6xHis tag.

MALQIPSLLLSAAVVVLMVLSSPGTEG/GDS**EAWGALANWAVDSA**GGGGSLVPRGSGGGGSERHFVYQFMGECYFTNGTQRIRYV
TRYIYNREEYVRYDSDVGEHRAVTELGRPDAEYWNSQPEILERTRAELDTVCRHNYEGPETHTSLRRLEQPNVVISLSRTEALNHHNTLV
CSVTDFYPAKIKVRWFRNGQEETVGVSSTQLIRNGDWTFQVLVMLEMTPRRGEVYTCHVEHPSLKSPITVEWRAQSESAWSKGGGGST
TAPSAQLKKKLQALKKKNAQLKWKLQALKKKLAQHHHHHH.

QUANTIFICATION AND STATISTICAL ANALYSIS

Data were analyzed using Prism software (GraphPad) and R (The R Project for Statistical Computing)[80]. Pairwise correlation statistics was performed using the Pearson correlation score. Significance testing was performed using the nonparametric Mann–Whitney test (two-tailed), one-way ANOVA with Bonferroni's multiple comparisons test (two-tailed), or Fisher's exact test, as specified in the figure legends. The number per group is indicated in the figure legends. A value of $p < 0.05$ was considered statistically significant.